Disrupted priming within draining lymph nodes drives immune quiescence in gastric cancer

Sohrab Salehi[1,2]*, Emily E. Stroobant[3]*, Hannah Lees[1]**, Ya-Hui Lin[4]**, Shoji Shimada[5]**, Miseker Abate[3,6]**, Matthew Zatzman[1], Nicholas Ceglia[1], Sam Freeman[1], Monika Laszkowska[7], Steven Maron[8], Andrew McPherson[1], Nicole Rusk[1], Eliyahu Havasov[1], Harrison Drebin[9], Ping Gu[8], Laura H. Tang[10], Yelena Y. Janjigian[8], Ruslan Soldatov[1], Ronan Chaligne[11], Sohrab P. Shah[1]***, Vivian E. Strong[3,6]***, Santosha A. Vardhana[4]***

*These authors contributed equally

** These authors contributed equally

***Co-corresponding

[1]The Halvorsen Center for Computational Oncology, Memorial Sloan Kettering Cancer Center, New York, NY, USA

[2] Irving Institute for Cancer Dynamics, Columbia University, New York, NY, USA.

[3]Gastric and Mixed Tumor Service, Department of Surgery, Memorial Sloan Kettering Cancer Center, New York, NY, USA.

[4]Human Oncology and Pathogenesis Program, Memorial Sloan Kettering Cancer Center, New York, NY, USA.

[5]Digestive Disease Center, Showa University, Northern Yokohama Hospital, Yokohama, Japan.

[6]Department of Surgery, New York-Presbyterian Hospital/Weill Cornell Medicine, New York, NY, USA.

25 [7]Gastroenterology, Hepatology, and Nutrition Service, Department of Medicine, Memorial Sloan
26 Kettering Cancer Center, New York, NY, USA.
27 [8]Gastrointestinal Oncology Service, Department of Medicine, Memorial Sloan Kettering Cancer
28 Center, New York, New York.
29 [9]Vagelos College of Physicians and Surgeons, Columbia University Irving Medical Center, New
30 York, NY, USA
31 [10]Department of Pathology, Memorial Sloan Kettering Cancer Center, New York, New York.
32 [11]Single-cell Analytics Innovation Laboratory, Memorial Sloan Kettering Cancer Center, New
33 York, NY, USA.
34 Correspondence: shahs3@mskcc.org, strongv@mskcc.org, vardhans@mskcc.org

Abstract

The gastric mucosa is characterized by continuous innate immune surveillance and inflammatory signaling, yet a high proportion of gastric carcinomas (GCs) are recalcitrant to immune-directed therapies. The mechanisms by which GCs evade adaptive immune surveillance within the highly antigenic microenvironment of the gastric mucosa remains unknown. To address this, we collected patient-matched tumor tissue, distant normal tissue, metastasis, and draining lymph nodes to generate a large-scale single-cell immune profiling dataset from 64 patients (n=179 samples, >150,000 cells). From single cell analysis, we identified two distinct sources of impaired tumor surveillance within tumor draining lymph nodes. First, we observed that a significant fraction of tumor draining lymph nodes had undergone cytokine-driven reprogramming, leading to reduced dendritic cell homing and limited T cell priming. Second, T cells undergoing successful activation exhibited limited expansion and constrained differentiation, marked by expression of the quiescence-associated transcription factor Kruppel-like Factor 2 (*KLF2*). Overexpression of *KLF2* in primary T cells limited both their differentiation and cytotoxic capacity. These findings implicate both impaired T cell priming and *KLF2*-dependent T cell quiescence in limiting T cell immunity in gastric adenocarcinoma. We suggest these findings represent an emerging model for immune silencing in tumors developing from tissues with chronic inflammation.

55 **Introduction**

56 Tumor growth and progression require evasion of immune surveillance; yet, paradoxically,
57 chronic inflammation is a well-established risk factor for multiple cancers. This dichotomy is
58 evident in gastric adenocarcinoma, a malignancy with rising global incidence and poor outcomes,
59 particularly once lymphatic or distant spread occurs[1]. The role of chronic inflammation in gastric
60 carcinogenesis was first established with the classification of *Helicobacter pylori* as a carcinogen
61 in 1994[2]. Subsequent associations with microbiota and autoimmune conditions further
62 positioned chronic inflammation as a central driver of gastric carcinogenesis[3-6]. Yet at clinical
63 diagnosis, most gastric cancers, and particularly those without evidence of microsatellite
64 instability, are thought to be immunologically silent with sparse infiltration of cytotoxic CD8+ T
65 lymphocytes (TILs)[7]. How chronic inflammation disrupts CD8+ T cell-dependent immune
66 surveillance remains unclear. We recently found that intra-tumoral T cell abundance in gastric
67 cancer correlates with effective T cell priming in gastric tumor-draining lymph nodes[8]. This led
68 us to hypothesize that chronic inflammation impairs adaptive immune surveillance by disrupting
69 T cell priming within draining lymph nodes. To test this hypothesis, we developed a surgical
70 collection protocol enabling paired profiling of immune cells from gastric tumors and matched
71 tumor-draining lymph nodes through integrated single-cell RNA sequencing, T-cell receptor
72 (TCR) sequencing and cell-surface epitope assessment (CITE-Seq)[9]. Our findings establish two
73 complementary mechanisms by which sustained innate inflammation disrupts anti-tumor T cell
74 immunity: by i) reducing the frequency of successful T cell priming events within draining lymph
75 nodes and ii) stabilizing transcriptional programs that reinforce T cell quiescence.

76

77 **Patient cohort, sample collection and single cell data generation**

78 To characterize adaptive immune networks during both the priming and effector stages of the
79 immune response, we developed a tissue collection protocol from patients with gastric
80 adenocarcinoma, emphasizing tumor resections paired with matched draining lymph nodes

81 (dLN) (**Fig. 1a**). 64 patients with gastric adenocarcinoma were included with patient tumor
82 characteristics broadly distributed across gastric cancer stages, subtypes and characteristics
83 (**Extended Data Table 1, 2**). This included at least eight patients from each tumor subtype by
84 Lauren classification[10], and representation from all TCGA subtypes[11] (**Fig. 1b**). Importantly, a
85 broad distribution of PD-L1 expression by combined positive score (CPS)[12] was also observed
86 (0-100), indicating that analyzed tumors represented a broad range of immunogenicity by
87 conventional metrics. Median follow-up was 2.5 years after initial specimen collection.
88
89 In total, 179 fresh tissue samples (74 tumor samples, 56 distant normal samples, 36 draining
90 lymph nodes, and 13 metastasis samples) were collected from patients undergoing clinically
91 indicated diagnostic laparoscopy (DL) with esophagogastroduodenoscopy (EGD) or
92 gastrectomy for gastric adenocarcinoma by a specialist gastric cancer surgeon (Methods,
93 section Sample Collection and Processing) (**Fig. 1a,b**). All samples were dissociated into single
94 cell suspensions and viably cryopreserved within 2.5 hours of resection. Subsequently, batches
95 of no more than 30 samples were thawed, barcoded, and stained for viability. Sorted viable cells
96 were multiplexed and profiled by CITE-Seq and single-cell TCR-Seq[13].
97
98 **Single cell immune profiling of gastric tumors and matched draining lymph nodes**
99 We first analyzed immune cell subsets from 152,981 CD45+ cells passing quality control (QC)
100 filtering (**Methods, section** *Single-Cell Analysis***, Extended Data Table 3**). Unsupervised graph-
101 based clustering identified six main CD45+ cell types marked by canonical identifying genes
102 (**Fig. 2a, Extended Fig. 1a**): 98,274 T/NK cells (*CD2, CD3D, CD3E*), 23,560 B cells (*CD19,*
103 *MS4A1*), 19,774 plasma cells (*JCHAIN, CD38*), 8,876 myeloid cells (*CD14, CD68, S100A9*),
104 1,687 mast cells (*KIT, TPSAB1*), and 810 plasmacytoid dendritic cells (DCs) (*IL3RA, CLEC4C*).
105

106 We then further subclustered CD8+ T cells (**Fig. 2b**), CD4+ T cells (**Fig. 2c**), and myeloid
107 cells/DCs (**Fig. 2d**) using a combination of known marker genes and surface proteins (**Extended**
108 **Data Table 4**). Classical CD8+ T cell phenotypes including naïve (*SELL, LEF1*), early activated
109 (*FOS, FOSB*), late activated (*HLA-DRA, HLA-DRB1*), effector (*CCL4, XCL1*), central memory
110 (*GZMK, CD28*), proliferating (*MKI67, TYMS*), early exhausted (*TOX, CTLA4*), progenitor
111 exhausted (*THEMIS, SLAMF6*), terminally exhausted (*LAG3, GZMB*), effector memory (*IL7R,*
112 *ID2*), heat shock protein (HSP) associated (*HSPA1A, HSPA1B),* and effector memory with
113 expression of CD45RA (EMRA) (*PRF1, NKG7*) subsets were identified, as well as a cluster of
114 CD8+ T cells marked by expression of *NEAT1* (*NEAT1, CBLB*) (**Extended Fig. 1b**). CD4+ T cell
115 phenotypes included naïve (*SELL, LEF1*), central memory (*CXCR4, CCR7*), effector memory
116 (*CXCR3, GPR183*), follicular helper (*CXCR5, BCL6*), cytotoxic (*PRF1, GZMB*), HSP-associated
117 (*HSPA1A, HSPA1B*), proliferating (*MKI67, TYMS*), and Th17 (*IL17A, RORC*) cells, as well as a
118 *NEAT1*-expressing cluster (*NEAT1, CBLB*) and two subsets of regulatory T cells (*FOXP3, TIGIT*)
119 (**Extended Fig. 1c**). A proliferative cluster was identified in both CD4+ and CD8+ T cells (*MKI67,*
120 *TOP2A*) (**Extended Fig. 1d**).
121
122 Within the myeloid compartment, we identified mast cells (*KIT, TPSAB1*) as well as dendritic cell
123 subsets including cDC1 (*CLEC9A, XCR1*), cDC2 (*CD1C, CLEC10A*), migratory DCs (*CCR7,*
124 *LAMP3*), and plasmacytoid DCs (*CLEC4C, LILRA4, TCF4*). We observed two macrophage
125 populations, distinguished by either NLRP3+ inflammasome activation (*NLRP3, IL1B, IL1RN*) or
126 expression of complement proteins (*C1QA, C1QB, C1QC*) (**Extended Fig. 1e**). CD8+ T cells
127 were the more abundant immune cell type within tumors, whereas CD4+ T cells dominated both
128 tumors and dLN (**Fig. 2a, Extended Fig. 1f**). Amongst CD8+ T cells, dLN primarily contained
129 naïve and central memory cells while tumors contained primarily activated, effector memory, and
130 exhausted T cells (**Fig. 2b**). CD4+ T cells within dLN were primarily naïve while tumors
131 contained a mix of regulatory, Th17, and cytotoxic CD4 T cells (**Fig. 2c**). Finally, within the

132 myeloid compartment, lymph nodes contained predominantly cDC2s and plasmacytoid DCs,
133 while tumors were marked by NLRP3 macrophages and mast cells (**Fig. 2d**). Heat maps for
134 normal and metastasis samples are in **Extended Fig. 2**. Lymph node and tumor samples were
135 primarily non-overlapping in all three cell compartments (CD8+, CD4+ and myeloid).
136

137 **Patient-specific immune networks defined by cytokine-driven cell-cell communication**

138 We set out to analyze how chronic inflammation influenced the distribution and interactions of
139 immune cells within gastric tumors and tumor-draining LN. Using a recently generated cytokine
140 dictionary of gene expression changes in individual immune cell types isolated from mice treated
141 with a library of 86 distinct cytokines[14] (**Fig. 3a**, **Methods,** section *Tensor factorization for*
142 *Cytokine Activation using IREA*), we quantified activation of gene expression programs
143 associated with cytokine exposure in each cell type from our cohort. Briefly, after mapping cell
144 types identified in **Fig. 2** to their murine counterparts, we computed cytokine enrichment in each
145 cell type using an over-representation analysis at the sample level (**Methods,** section *Tensor*
146 *factorization for Cytokine Activation using IREA*). We then applied a Bayesian sparse tensor
147 factorization approach, effectively modeling variation in cytokine-driven expression programs
148 across samples. This resulted in five robustly enumerated factors, with model weights in both
149 'receiver' cell-type and 'cytokine' activation dimensions (**Extended Fig. 3a**). Factor 0 was
150 strongly associated with cDC2 activation, and moderately with pDCs. Factor 1 was strongly
151 associated with Treg activation, and (γδ) T cells. Factor 2 was associated with CD4 T cells and
152 Tregs, Factor 3 with macrophages, and Factor 4 with CD8+ T cells, NK cells, and B cells. Factors
153 0 and 2 were enriched in the dLN, while Factors 3 and 4 were enriched in the tumor; this is
154 consistent with dendritic cell and CD4+ T cell abundance within lymph nodes, and macrophage
155 and CD8+ T cell abundance within tumors. Regarding cytokines, IL1a was enriched in Factor 2
156 while IL15 and TNFa were enriched in Factor 3. IL1 alarmin was the highest activated cytokine
157 family in Factors 1, 2, and 3, while Factors 0 and 4 were more balanced with the highest activity

158 from the IL2 family. Growth factors and receptor antagonists were the least activated cytokine
159 families across all Factors.
160
161 We next stratified tumor and dLN samples by factor enrichment. This process yielded two
162 clusters of cytokine-driven immune networks in dLN, and 3 clusters in tumors (**Methods**, section
163 *Clustering of samples based on IREA scores*) (**Fig. 3b**). One dLN cluster ("canonical" LN) was
164 defined by crosstalk between classical dendritic cells and T cells. Consistent with intact LN
165 priming events, central memory CD8+ T cells, follicular helper CD4+ T cells, and type 2 and
166 plasmacytoid dendritic cells were prevalent in this cluster (**Fig. 3c**, **Extended Fig. 3b**). The
167 second dLN cluster ("disrupted" LN) showed a decrease in cytokine-driven transcriptional activity,
168 with macrophages as the dominant cytokine-responsive cell type (**Fig. 3c**, **Extended Fig. 3b**).
169 Notably this cluster harbored an abundance of CD8+ and CD4+ T cells with a naïve phenotype
170 (**Extended Fig. 3b**) and macrophages with an NLRP3+ phenotype (**Fig. 3c**). Given the relative
171 dominance of macrophage-driven crosstalk and the absence of dendritic cells needed for
172 classical T cell priming, we labeled LN within this cluster as "disrupted". Tumor clusters were
173 similarly interpreted based on cytokine-driven immune cell interactions, with "T cell engaged"
174 dominated by high-strength T cell interactions, activated and exhausted CD8+ T cells, and Th17
175 CD4+ T cells, "inflamed myeloid" with primarily NLRP3+ macrophage driven interactions, and
176 "immune silent" with minimal immune cell infiltration or cytokine-driven interactions (**Fig. 3c,**
177 **Extended Fig. 3b**).
178
179 We next asked which ligand-receptor interactions contributed most strongly to these cytokine-
180 driven phenotypes. We inferred intercellular ligand-receptor (L-R) interactions, with a focus on
181 cytokine-driven L-R interactions[15,16] (**Methods,** section *Receptor Ligand activation analysis*).
182 Inference of interactions was consistent with dendritic cells as the dominant target of cytokine-
183 driven L-R interactions within canonical LN, integrating signals from several immune cell subsets.

184 Analogously, macrophages were the dominant source of cytokine-driven L-R interactions,
185 broadly targeting immune cell subsets within disrupted LN (**Fig. 3d**). Transforming growth factor
186 beta (*TGFB1*) was the dominant source of cytokine-mediated crosstalk within canonical LN,
187 whereas several innate inflammatory cytokines, including IL-1 (*IL1A, IL1B*) and TNF, dominated
188 cytokine-mediated crosstalk in disrupted LN samples (**Fig. 3d**).
189
190 We then explored whether paired tumors and their dLN showed co-varying cytokine-driven
191 reprogramming. The two dLN types led to significantly different tumor type distributions (p-value
192 = 0.04, chi-squared test); canonical dLN were more often paired with T-cell engaged tumors,
193 while disrupted dLN were more often paired with either immune silent or inflamed myeloid tumors
194 (**Fig. 3e**). Individual patient tumor and dLN types are listed in **Extended Data Table 5**. There
195 was no clear correlation of genomic features with either tumor or dLN type (**Extended Fig. 3c**).
196 Interestingly, there was an uneven distribution amongst traditional tumor types, with diffuse-type
197 tumors, which carry the poorest prognosis amongst gastric tumor subtypes[17], pairing exclusively
198 with disrupted dLN (**Fig. 3f**). As T cell priming occurs in the lymph node, these results suggest
199 that altered priming within dLN contributes to the lack of intratumoral T cell surveillance in these
200 tumor subtypes.
201 **Reduced T cell priming in disrupted tumor draining lymph nodes**
202 Linked cytokine-driven reprogramming between tumor and matched dLN suggests that chronic
203 inflammation-driven loss of dendritic cell homing to disrupted dLN might impair adaptive immune
204 responses. To investigate this, we next focused on the impact of canonical and disrupted dLN
205 on CD8+ T cell phenotypic trajectories. We generated a CD8+ T cell trajectory manifold
206 (**Methods**, section *CD8+ T cell Trajectory Analysis*) and mapped T cells according to their
207 transcriptional phenotypes (**Fig. 4a**). T cells from dLN and tumors had limited phenotypic overlap
208 (**Fig. 4b**). A computational fate analysis (**Methods**, section *CD8+ T cell Trajectory Analysis*)
209 revealed 6 primary terminal states for naïve CD8+ T cells, including activated, effector, EMRA,

210 Neat1+, and proliferating fates, as well as a cell fate in which T cells remained in a naïve-like
211 state (**Fig. 4c**). Using single-cell TCR analysis, we confirmed that clonally expanded T cells were
212 mostly, though not exclusively in the tumor, with clonally expanded T cells within the tumor
213 occupying a wide distribution of effector and exhausted states and expanded T cells within the
214 LN occupying primarily a central memory state (**Extended Fig. 4a**).
215
216 We next asked whether T cell trajectories were altered by canonical versus disrupted lymph
217 node priming by mapping T cell trajectories between canonical and disrupted LN and their most
218 frequent paired tumor states. In canonical LN-tumor pairs, dLN CD8+ T cells were primarily of
219 a central memory phenotype and could be found within all six terminal states within the tumor.
220 In sharp contrast, T cells from disrupted LN-tumor pairs were primarily phenotypically naïve
221 within the dLN, and their intratumoral trajectories were substantially more restricted (**Fig. 4d**).
222 This constrained differentiation could be directly attributable to altered priming within the dLN,
223 as TCR analysis revealed that CD8+ T cells within disrupted LN displayed reduced clonal
224 expansion and a reduced phenotypic entropy (**Fig. 4e**), with the majority of CD8+ T cells
225 occupying either a naïve or EMRA phenotypic state (**Fig. 4f**).
226 Curiously, a fraction of phenotypically naïve CD8+ T cells from disrupted dLN downregulated
227 surface expression of CD45RA, which typically occurs in the context of antigen experience[18,19]
228 (**Fig. 4g**), despite being transcriptionally similar to naïve cells (**Fig. 4h**). We therefore stratified
229 phenotypically naïve T cells based on CD45 isoform expression (CD45RA vs. CD45RO,
230 included in our CITE-seq antibody-derived tags (ADT) panel). Phenotypically naïve T cells
231 negative for CD45RA and positive for CD45RO ('$RA^{-}RO^{+}$') showed signs of antigen experience
232 on the protein level, including downregulation of L-selectin and CD3[20,21], as well as upregulation
233 of Fas[22], consistent with being recently activated. In contrast, T cells negative for CD45RA and
234 CD45RO ('$RA^{-}RO^{-}$') largely overlapped with CD45RA+, CD45RO- canonically naïve T cells, with
235 sustained expression of L-selectin and CD3 (**Fig. 4i**). Trajectory analysis of these 3

236 phenotypically naïve T cell subsets along with early activated T cells confirmed that RA^-RO^- T
237 cells were similar to RA^+RO^-naïve T cells, whereas RA^-RO^+ cells were more similar to early
238 activated T cells (**Fig 4j, Extended Fig. 4b**). We therefore combined double negative RA^-RO^- T
239 cells with RA^+RO^- true naïve cells and RA^-RO^+ cells with early activated T cells for downstream
240 analysis. We found that compared to canonical dLN, T cells within disrupted dLN were enriched
241 in either a naïve or EMRA phenotype, indicating that inflammatory reprogramming of disrupted
242 dLN is sufficient to limit T cell priming and downstream tumor surveillance (**Extended Fig. 4c**).
243

244 **KLF2 suppresses effector T cell differentiation in gastric tumor-draining LN**

245 Despite showing increased clonal expansion relative to T cells from disrupted LN, T cells from
246 canonical LN also showed evidence of phenotypic constraint, with the majority of clonally
247 expanded T cells within dLN remaining in a central memory state (**Extended Fig. 5a**). To identify
248 transcriptional regulators that might restrict differentiation and egress of CD8+ T cells from dLN,
249 we analyzed expression of transcription factors in clonally expanded CD8+ T cells compared
250 with clonally expanded T cells from tumors. We found that Kruppel-like Factor-2 (*KLF2*)[23] was
251 the most differentially upregulated transcription factor in clonally expanded T cells retained within
252 dLN (**Fig. 5a**). Within both dLN and tumors, *KLF2* expression correlated strongly with expression
253 of genes linked to quiescence (*LEF1, TCF7*) and LN retention (*S1PR1, S1PR4, CCR7, SELL*)
254 and inversely with genes linked to tissue infiltration (*ITGAE*, *CXCR6*) and effector function (*IRF4,*
255 *GZMB*) (**Fig 5b**). Moreover, *KLF2* expression inversely correlated with clone size amongst
256 expanded clones within the LN and tumor, suggesting that *KLF2* expression may reinforce
257 quiescence and LN retention while restricting T cell expansion, differentiation, and LN egress
258 (**Fig. 5c**).
259

260 To directly assess the consequences of *KLF2* stabilization on T cell activation and differentiation,
261 we transduced activated primary human T cells with either lentivirus encoding *KLF2* or a vector

262 control (**Extended Fig. 5b**) and interrogated cells using a combination of flow cytometry and
263 combined single-cell RNA and ATAC sequencing (DOGMA-Seq)[24]. *In vitro* activated T cells
264 differentiated into several T cell states marked by distinct transcriptional modules, including
265 proliferating, effector, effector memory, and central memory T cells, with a minority of T cells
266 occupying innate-like, activated, or intermediate states (**Fig 5d, Extended Fig. 5c**). Naïve cells
267 were not present as T cells had been previously activated to facilitate lentiviral transduction.
268 Consistent with *KLF2* expression and accessibility marking a central memory phenotype[25], we
269 found that overexpression of *KLF2* in primary T cells led to an increased abundance of CD8+ T
270 cells with a central memory phenotype and a decreased abundance of T cells with an effector
271 memory phenotype (**Fig. 5e,f**). To determine the mechanism by which *KLF2* alters T cell
272 differentiation, we identified differentially accessible motifs in central memory versus effector
273 memory T cells using ChromVar[26]. We found that CCCTC-binding factor (*CTCF*) and Interferon
274 Regulatory Factor (*IRF*) motif accessibility were associated with effector memory T cells,
275 whereas *FOXO1* and T-box (*TBX*) family members were associated with central memory T cells
276 (**Fig. 5g**). Measurement of promoter-centered chromatin accessibility confirmed that promoter-
277 associated accessibility of both *CTCF* and *IRF* transcription factors was reduced in *KLF2*-
278 overexpressing cells (**Fig. 5h**). As both *CTCF* and *IRF* transcription factors are known to be
279 required for effector CD8+ T cell differentiation[27-32], we measured both effector T cell
280 differentiation and cytotoxic function and found them to be reduced in *KLF2* overexpressing T
281 cells (**Fig 5i, Extended Fig. 5d**).
282
283 Finally, to identify potential mechanisms by which *KLF2* might limit T cell differentiation and
284 tumor infiltration, we identified putative *KLF2* target genes by asking which genes containing a
285 KLF-binding motif[33] (CCACGCCC) were differentially expressed in *KLF2* versus vector
286 overexpressing CD8+ T cells. *KLF2* overexpression was associated with reduced expression of
287 target genes associated with effector memory T cells, such as *TOX*, *TOX2*, and *ITGAE* and

288 increased expression of the GTPase activating proteins (GAP) *RAPGAP2* and *RASA3* (**Fig. 5j**).
289 *RAPGAP2* and *RASA3* bind and stimulate the catalytic activity of the Rap1 GTPase[34-36]. Rap1
290 has been shown to be required for the TCR-dependent conformational change in Lymphocyte
291 function-associated antigen-1 (LFA-1) that enables interaction with its ligands, otherwise known
292 as 'inside out' signaling. This led us to hypothesize that *KLF2*-driven expression of Rap1 GAPs
293 may limit T cell priming by disrupting LFA-1 activation. Consistent with this hypothesis, surface
294 expression of both components of the LFA-1 heterodimer (CD11a and CD18) was reduced in
295 naïve and central memory T cells from disrupted LN; moreover, *KLF2* expression *in vitro* was
296 sufficient to lower expression levels of CD11a and CD18 when compared to our empty vector
297 control (**Fig. 5k**). To directly test the impact of LFA-1 activity on T cell priming and differentiation,
298 we activated OT-I TCR transgenic T cells with cognate peptide across a range of antigen dose
299 and affinities using altered peptide ligands of the canonical OT-I TCR cognate peptide SIINFEKL
300 (**Extended Fig. 6a**). Addition of LFA-1 blocking antibodies during T cell priming by peptide-
301 pulsed DCs increased the threshold for activation, proliferation, and effector function across
302 peptide doses and affinities, providing a mechanism by which *KLF2* stabilization influences both
303 T cell priming and effector differentiation in GC (**Extended Fig. 6b,c**).
304

305 **Cytokine driven dLN types are not fixed**

306 Lymph nodes are typically only surgically resected during gastrectomy, as a fundamental part of
307 staging. However, for one specific patient (GC028) a biopsy of a visible draining lymph node
308 was collected during diagnostic laparoscopy (DL) for evaluation of metastatic gastric cancer as
309 well as during surgical resection after achieving a near complete response to neoadjuvant
310 chemotherapy (FOLFOX)[37] (**Fig. 6a**). This unique pairing of tumor and draining lymph node both
311 before and after neoadjuvant chemotherapy allowed us to investigate whether cytokine driven
312 dLN types remain fixed. Classification of both pre-treatment and post-treatment samples based
313 on cytokine networks revealed a disrupted dLN prior to treatment and a canonical dLN at the

314 time of resection (**Fig. 6b**). Accordingly, the post-treatment dLN showed a decreased abundance
315 of C1QC+ macrophages and an increased abundance of plasmacytoid DCs (**Fig. 6c, Extended**
316 **Fig. 7a**).
317
318 Clonotype tracking between the dLN and tumor pairs revealed that shared clones were present
319 between all 4 samples (**Extended Fig. 7b**). Phenotypes of shared CD8+ T cell TCR clonotypes
320 changed post-treatment, with an increase in the fraction of progenitor Texh in the tumor and CM
321 in the dLN (**Extended Fig. 7c**). The post-treatment canonical dLN also had both a larger number
322 of expanded clones and a greater diversity of expanded T cell phenotypes from the dLN to its
323 paired tumor (**Fig. 6d**). We examined overall *KLF2* expression in CD8+ T cells in the pre-therapy
324 disrupted dLN and the post-therapy canonical dLN and found that *KLF2* expression was
325 significantly higher in the disrupted dLN (pre) than the canonical dLN (post) (**Fig. 6e**). *KLF2* was
326 also the second most transcriptionally decreased gene between these pre-treatment and post-
327 treatment dLN (**Extended Fig. 7d**). In line with this evidence, expression of both LFA-1
328 components (CD11a and CD18) was increased in the canonical dLN (post-treatment)
329 (**Extended Fig. 7e**). The ability for tumor draining lymph nodes to change from disrupted to
330 canonical types, paired with changes in *KLF2* expression, reveals that cytokine driven dLN types
331 can respond to therapeutic intervention and may have prognostic implications, as this patient
332 remains in complete remission 2.7 years after diagnosis despite presenting with metastatic
333 disease.
334
335 **Discussion**
336 The paradoxical role of the immune responses in tumorigenesis is evidenced by decades of
337 epidemiologic studies demonstrating an increased risk of cancers in both immunocompromised
338 patients and patients with autoimmune conditions[38-41]. This archetype is exemplified by gastric
339 cancer, where chronic inflammation is a well-established driver of carcinogenesis, yet most

340 gastric tumors show limited evidence of T cell surveillance. Here we provide a novel mechanistic
341 explanation for how persistent innate inflammation can impair anti-tumor T cell immunity.
342 Chronic inflammation limits dendritic cell accumulation within tumor draining lymph nodes,
343 preventing exposure of putatively tumor-reactive naïve T cells within the lymph node to tumor-
344 derived neoantigens. Whether targeting innate inflammatory signaling can enhance DC homing
345 and T cell priming represents an important area for future investigation.
346
347 We also identify a second, previously unappreciated checkpoint on T cell surveillance in gastric
348 cancer. Activated T cells within the draining LN largely fail to differentiate into effectors, instead
349 becoming central memory T cells that remain in the LN and express high levels of *KLF2*. This
350 may be in part due to reduced integrin activity increasing the threshold for T cell activation during
351 naïve T cell priming events within dLN. These findings are consistent with recent evidence
352 demonstrating a role for *KLF2* in preventing T cell exhaustion[42]. By suppressing the exhaustion
353 program, *KLF2* may paradoxically reduce the clinical efficacy of immune checkpoint inhibitors
354 that target inhibitory receptors preferentially expressed on exhausted T cells, including PD-1,
355 CTLA-4, and LAG-3. Future studies to determine if *KLF2* expression in T cells is associated
356 with lack of immune checkpoint blockade (ICB) response or whether targeting either *KLF2* or
357 *KLF2*-dependent integrin activation can enhance sensitivity to ICB would have immediate clinical
358 relevance.
359
360 Our findings provide insights into how reciprocal balances between innate and adaptive immune
361 responses maintain homeostasis in an inflammatory microenvironment, and how an imbalance
362 between these responses contributes to human disease. The extent to which the T cell
363 phenotypes observed in this study apply to other tumor types remains unknown. However, this
364 unique dataset, derived from prospective surgical sampling of paired tumors and draining LN,
365 may serve as a valuable reference to understand whether lymph node priming is disrupted in

366 other cancers. Blunting of the adaptive immune response during chronic inflammation may
367 represent a physiologic mechanism to preserve mucosal tolerance and barrier integrity;
368 consistent with this hypothesis, T cell specific *KLF2* expression is required to maintain
369 commensal tolerance and prevent inflammatory bowel disease[43]. However, adaptive immune
370 suppression has been reported in other chronic inflammatory conditions, including sepsis-
371 associated immune paralysis[44]. Potential targets such as *KLF2* may enable T cells to escape
372 from this maladaptive state, and the ability for dLN to change with intervention further supports
373 tumor draining lymph nodes as a viable focus for therapeutic development. Anecdotally, our
374 report of a patient with pre- and post-treatment tissue collections demonstrating phenotypic T
375 cell state transitions linked to a remarkable clinical response indicates that the non-canonical
376 immune states we describe in this study are potentially reversible with therapeutic intervention.
377 Characterizing the prevalence and determinants of such immune state transitions will be central
378 to future translational efforts aimed at enhancing lymph node priming in gastric cancer.

379 **Figure Legends**

380

381 **Figure 1**. **Patient cohort and sample collection.** (a) Schematic of surgical sample collection
382 from gastric cancer patients and processing for scRNA-seq. (b) Swimmer's plot showing
383 individual patients with samples collected, tumor characteristics, and simplified patient timelines.

384

385 **Figure 2: Single cell characterization of immune cells from primary tumor, distal normal,**
386 **draining lymph nodes, and metastases in GC.** Uniform manifold approximation and
387 projections **(**UMAP) depicting (a) broad CD45+ cell subsets (left), density heatmap of CD45+
388 cells from dLN (center) and tumors (right), (b) CD8+ T cell subsets (left), density heatmap of
389 CD8+ cells from dLN (center) and tumors (right), (c) CD4+ T cell subsets (left), density heatmap
390 of CD4+ cells from dLN (center) and tumors (right), and (d) myeloid cell subsets (left), density
391 heatmap of myeloid cells from dLN (center) and tumors (right).

392

393 **Figure 3**. **Patient stratification by distinct cytokine driven immune networks in tumors and**
394 **their draining lymph nodes.** (a) Workflow of sample level Bayesian sparse tensor
395 decomposition. (b) Clustering of individual patient samples from dLN (left) and tumors (right)
396 based on sparse tensor decomposition from (a). (c) Summary of enriched cytokine-cell type
397 interactions in dLN and tumor subtypes with UMAPs showing the fraction of myeloid cell type
398 content and paired myeloid cell density. (d) Dominant cell type-specific receptor-ligand
399 interactions identified using CellChat in canonical and disrupted dLN subtypes. (e) Correlation
400 of cytokine interaction-dependent dLN and tumor subtypes in patients with paired samples
401 demonstrates a significant association between dLN and tumor types as indicated (p-value =
402 0.04, chi-squared test) (f) Distribution of Lauren and molecular subtypes across paired dLN-
403 Tumor networks.

404

405 **Figure 4**. **Reduced T cell priming in disrupted tumor draining lymph nodes.** (a-d) Trajectory
406 manifold of CD8+ T cell subsets across dLN and tumor, showing distribution of (a) CD8+ T cell
407 subsets, (b) distribution within dLN and tumors, (c) fate probabilities, and (d) density mapping of
408 cells from 'disrupted-immune silent' pairs and 'canonical-T cell engaged' pairs. (e) Fraction of
409 shared expanded (clonotypes >20) CD8+ T cell clones between dLN and Tumor (left) and
410 average phenotype entropy in CD8+ T cells (right) (**Methods**, section *Phenotype entropy*),
411 stratified by canonical dLN versus disrupted dLN. (f) Difference in mean cell fractions of CD8+
412 T cell subsets between disrupted dLN and canonical dLN. (g) Surface CD45 isoform expression
413 distribution on CD8+ T cells from disrupted dLN with a transcriptionally naïve phenotype. (h)
414 Cells from (g) projected on the trajectory manifold from (a), coded by CD45 isoform expression.
415 (i) Expression of genes and proteins associated with T cell activation on phenotypically naïve T
416 cells from (g,h), stratified by surface expression of CD45 isoforms. (j) Density heatmaps of
417 subtypes of naïve cells from (g-i), projected onto the CD8+ trajectory manifold from (a).
418
419 **Figure 5**. **KLF2 suppresses effector T cell differentiation.** (a) Differentially expressed
420 transcription factors expressed in non-naïve CD8+ T cells from tumors (up) vs. dLN (down). (b)
421 Genes correlated with the KLF2 expression in non-naïve CD8+ T cells across tumors and dLN
422 (c) Correlation of KLF2 expression on non-naïve CD8+ T cells across tumors and dLN with
423 clonotype size. (d) UMAP of activated human CD8+ T cells transduced with either empty vector
424 or a KLF2 overexpression vector. (e) Density plot showing relative distribution of CD8+ T cell
425 phenotypes in primary human CD8+ T cells transduced with either empty vector (left) or KLF2
426 overexpressing vector (right). (f) Mean fraction of T cell subsets in primary human CD8+ T cells
427 transduced with either empty vector or KLF2 overexpressing vector as indicated. (g)
428 Transcription factor motifs with top accessibility scores in central memory (right) compared with
429 effector memory (left) T cell subsets. (h) Volcano plot demonstrating accessibility of CTCF/L
430 (left) or IRF4/8 (right) motifs, centered around the transcriptional start site, in human CD8+ T

431 cells transduced with empty vector or KLF2 overexpression vector. (i) Expression of CXCR6 and
432 PD-1 (left) and intracellular accumulation of IFN-g and TNF following restimulation with PMA and
433 ionomycin in CD4+ and CD8+ T cells transduced with empty vector or KLF2 overexpression
434 vector. *ADT* antibody-derived tags (j) Relative expression of genes (KLF2 overexpression vector
435 vs. Empty vector) with an overlapping KLF2 motif (k) Differential surface expression of the LFA-
436 1 subunits CD11a and CD18 in indicated CD8+ T cell subsets from dLN, stratified by canonical
437 vs. disrupted dLN phenotype (left) and in primary human T cells transduced with empty vector
438 or KLF2 overexpression vector.
439
440 **Figure 6**. **Cytokine driven dLN types are not fixed.** (a) Patient timeline with tumor and LN
441 collection pre- and post-neoadjuvant chemotherapy treatment. (b) UMAP projections of myeloid
442 cells (left) and CD8+ T cells (right) for patient GC028 across both pre-treatment and post-
443 treatment conditions, colored by either cell subset or distribution in tumors and dLN. (c) Heat-
444 encoded density embeddings of myeloid and CD8+ T cell compartments prior to and following
445 neoadjuvant treatment, stratified by timepoint and anatomical site. (d) Alluvial plots showing
446 CD8+ T cells with shared TCRs across dLN and tumor, both pre- and post-treatment (e) KLF2
447 expression in CD8+ T cells within dLN of patient GC028, pre- and post-treatment.
448
449
450 **Extended Figure Legends**
451
452 **Extended Figure 1**. **Marker genes for major CD45+ cell compartments.** The expression of
453 marker genes in each major CD45+ cell compartment (a), CD8+ T cells (b), CD4+ T cells (c),
454 cycling cells in CD4+ and CD8+ T cells (d) and myeloid cells (e). (f) Fraction of cells in the major
455 CD45+ cell compartments within tumors and dLN as indicated.
456

457 **Extended Figure 2**. **Single cell characterization of immune cells from normal tissue and**
458 **metastatic sites in GC.** UMAPs depicting (a) broad CD45+ cell subsets across tissue sites (left),
459 density heatmap of CD45+ cells from distant normal tissue (center) and metastases (right), (b)
460 CD8+ T cell subsets across tissue sites (left), density heatmap of CD8+ cells from distant normal
461 tissue (center) and metastases (right), (c) CD4+ T cell subsets across tissues (left), density
462 heatmap of CD4+ cells from distant normal tissue (center) and metastases (right), and (d)
463 myeloid cell subsets across tissue sites (left), density heatmap of myeloid cells from distant
464 normal tissue (center) and tumors (right).
465
466
467 **Extended Figure 3**. **Patient stratification by distinct cytokine driven immune networks in**
468 **tumors and their draining lymph nodes.** (a) Posterior mean for latent sample by factor (left),
469 cell-type by factor (center), and cytokine by factor (right) tensor slices. For visualization purposes,
470 the cytokine by factor slide heatmap includes only cytokines with an average factor activation
471 score of more than 0.2. (b) UMAPs showing the fraction of CD8+ T cell type content and paired
472 CD8+ T cell density (left) and fraction of CD4 and myeloid cell subsets in each cytokine
473 interaction-driven immune network cluster. (c) Oncoplot of tumor mutation, separated by either
474 dLN or tumor subtype.
475
476 **Extended Figure 4**. **CD8+ T cell expansion.** (a) CD8+ T cell clonotype size distribution in dLN
477 and Tumor (left) and cell phenotypes for expanded TCR clonotypes (right). (b) Average distance
478 of naïve like T cells from non-naïve T cell phenotypes indicating closer proximity of RA-RO+
479 naïve T cells to early activated T cells (**Methods**, section *Distance between T Cell Phenotypes*).
480 (c) Difference in mean cell fractions of CD8+ T cell subsets between disrupted dLN and

481 canonical dLN following recategorization of naïve-like CD8+ T cells (RA^+RO^- naïve and RA^-RO^-
482 naïve into 'naïve merged', RA^-RO^+ naïve and early activated into 'early activated merged').
483
484 **Extended Figure 5**. **KLF2 suppresses effector T cell differentiation.** (a) Fraction of CD8+ T
485 cell phenotypes in expanded TCR clonotypes in each cytokine-driven immune network cluster.
486 (b) Western blot showing KLF2 and Histone H3 (loading control) protein abundance in primary
487 activated human T cells transduced with either empty vector control or KLF2 overexpression
488 vector. (c) Marker genes and their expression in CD8+ T cell phenotypes reported in empty
489 vector and KLF2 overexpression vector-transduced cells from **Fig. 5d**. (d) Flow cytometry gating
490 for **Fig. 5i**.
491
492 **Extended Figure 6. LFA-1 blockade attenuates T cell priming and effector differentiation.**
493 (a) Experimental design to assess the contribution of LFA-1 to DC-mediated T cell priming and
494 effector differentiation. (b) Flow cytometry scatter plots and gating of live, $B220^-NK1.1^-$
495 $TCRb^+CD8^+$ T cells to assess T cell activation ($CD69^+CD25^+$), proliferation ($CD44^+$CellTrace
496 $Violet^{low}$), effector differentiation ($CX3CR1^-CXCR6^+$) and cytokine production ($TNF^+IFN\text{-}g^+$). (c)
497 Quantitation of impact of peptide dose and affinity on CD8+ T cell activation, proliferation,
498 effector differentiation, and cytokine production as described in (b). Each **table entry** represents
499 the **average** of three independent biological replicates for each peptide affinity and dose.
500
501 **Extended Figure 7**. **Cytokine driven dLN types are not fixed** (a) Fraction of CD8+ T (left) and
502 myeloid cell type subsets (right) in patient GC0028, stratified by tissue (dLN and tumor) as well
503 as timepoint (pre- and post-treatment) (b) Abundance of TCR clonotypes that are shared across
504 time and anatomical sites (left) and their projection onto the patient GC0028-specific CD8+ T
505 cell UMAP (right) (c) Alluvial plots showing phenotypes of CD8+ T cells with shared TCR pre-
506 and post-treatment in both dLN (left) and tumor (right) samples. (d) Differentially expressed

507 genes in the dLN pre-treatment (up) vs post-treatment (down). (e) Expression of CD11a and

508 CD18 in CD8+ T cells from patient GC0028 dLN pre- and post-treatment.

509

510 **EXTENDED DATA TABLES**

511 **Extended Data Table 1**: Individual patient and tumor characteristics

GC#	pT-stage	pN-stage	pM-stage	Combined Tumor Subtype	*H. Pylori* History	Histological Grade	TRG	PDL1 CPS	HER2 Status	Therapy Prior to First Collection	Any Chemotherapy	Any Immunotherapy	Any Trastuzumab
GC001	ypT3	ypN2	M0	Mixed	Yes	poorly differentiated	3	1	negative	neoadj chemo	Yes	No	No
GC002	ypT3	ypN0	M0	Intestinal	No	moderately differentiated	3	50	negative	neoadj chemo	Yes	No	No
GC003	ypT3	ypN1	M0	Mixed	No	moderately to poorly differentiated		15	positive	No	Yes	Yes	No
GC004	pT1b	pN2	M0	Mixed	No	moderately differentiated		3	negative	No	Yes	No	No
GC005	Tx	Nx	M1	Diffuse	No	poorly differentiated		2	negative	No	Yes	Yes	No
GC006	Tx	Nx	M1	NA	No	poorly differentiated		5	NP	No	Yes	Yes	No
GC007	ypT0	ypN0	M0	NA	No	moderately differentiated		2	negative	No	Yes	Yes	No
GC008	Tx	Nx	M1	Diffuse	No	poorly differentiated		2	negative	chemo	Yes	Yes	No

GC009	ypT1a	ypN0	M0	Intestinal	No	moderately differentiated	2	10	negative	neoadj chemo	Yes	No	No
GC010	ypT3	ypN3	M0	Mixed	Yes	poorly differentiated		2	positive	neoadj chemo	Yes	No	No
GC011	ypT3	ypN0	M0	MSI-H	No	moderately differentiated	2	15	negative	neoadj chemo	Yes	No	No
GC012	Tx	Nx	M1	Diffuse	Yes	poorly differentiated		1	negative	neoadj chemo, adj chemo	Yes	No	No
GC013	Tx	Nx	M1	NA	No	poorly differentiated		20	negative	No	Yes	Yes	No
GC014	ypT3	ypN0	M0	Intestinal	No	poorly differentiated	3	0	negative	neoadj chemo	Yes	No	No
GC015	ypT4a	ypN3	M0	MSI-H	No	poorly differentiated		0	negative	No	Yes	No	No
GC016	ypT3	ypN0	M0	Mixed	Yes	poorly differentiated	2	0	negative	neoadj chemo	Yes	No	No
GC017	pT3	pN1	M0	Diffuse	No	poorly differentiated		1	negative	No	No	No	No
GC018	Tx	Nx	M1	MSI-H	No	poorly differentiated		25	negative	immuno	No	Yes	No
GC019	Tx	Nx	M1	NA	No	poorly differentiated		0	negative	No	Yes	No	No
GC020	Tx	Nx	M0	MSI-H	No	moderately to poorly differentiated		15	negative	No	Yes	Yes	No

GC021	Tx	Nx	M1	Intestinal	Yes	NA		0	positive	No	Yes	Yes	Yes
GC022	pT1b	pN0	M0	Intestinal	No	moderately differentiated		5	negative	No	No	No	No
GC023	Tx	Nx	M1	Diffuse	No	poorly differentiated		1	negative	No	Yes	Yes	No
GC024	pT1b	pN1	M0	Intestinal	Yes	moderately differentiated		35	negative	No	No	No	No
GC025	Tx	Nx	M1	NA	No	poorly differentiated		1	negative	No	Yes	No	No
GC026	pT1b	pN0	M0	NA	No	moderately differentiated		0	negative	No	Yes	No	No
GC027	ypT4b	ypN3	M0	EBV	No	poorly differentiated	3	15	negative	neoadj chemo	Yes	Yes	No
GC028	ypT3	ypN1	M1	Intestinal	Yes	NA		0	negative	No	Yes	No	No
GC029	pT2	pN0	M0	Mixed	No	poorly differentiated		1	negative	No	No	No	No
GC030	pT2	pN1	M0	MSI-H	Yes	poorly differentiated		1	negative	No	No	No	No
GC031	pT1a	pN0	M0	Intestinal	No	moderately differentiated		2	negative	No	No	No	No
GC032	Tx	Nx	M1	Diffuse	No	poorly differentiated		0	negative	No	Yes	Yes	No
GC033	ypT4a	ypN3	M0	Diffuse	No	poorly differentiated	3	1	negative	neoadj chemo	Yes	Yes	No

GC034	pT4a	pN2	M0	Mixed	Yes	poorly differentiated		0	negative	No	Yes	No	No
GC035	pT4a	pN0	M0	Diffuse	Yes	poorly differentiated		0	negative	No	Yes	No	No
GC036	ypT2	ypN0	M0	EBV	No	poorly differentiated	2	100	negative	neoadj chemo	Yes	No	No
GC037	ypT1b	ypN0	M0	Intestinal	No	moderately differentiated	1	1	positive	neoadj chemo	Yes	No	No
GC038	pT1a	pN0	M0	Intestinal	No	well differentiated		0	NP	No	No	No	No
GC039	ypT3	ypN0	M0	NA	No	poorly differentiated	2	0	negative	neoadj chemo	Yes	No	No
GC040	ypT1b	ypN0	M0	Intestinal	Yes	moderately to poorly differentiated	3	2	negative	neoadj chemo	Yes	No	No
GC041	pT1a	pN0	M0	Diffuse	Yes	poorly differentiated		0	negative	No	No	No	No
GC042	Tx	Nx	M0	MSI-H	No	NA		20	negative	No	No	Yes	No
GC043	Tx	Nx	M1	NA	No	moderately differentiated		30	negative	No	No	No	No
GC044	pT1b	pN0	M0	MSI-H	No	moderately to poorly differentiated		5	negative	No	No	No	No
GC045	pT3	pN0	M0	Diffuse	No	poorly differentiated		0	negative	No	Yes	No	No

GC046	Tx	Nx	M1	NA	No	moderately to poorly differentiated		0	negative	neoadj chemo	Yes	No	No
GC047	ypT3	ypN2	M0	NA	No	NA		1	negative	No	Yes	Yes	No
GC048	Tx	Nx	M1	NA	No	poorly differentiated		10	negative	chemo+immuno	Yes	Yes	No
GC049	Tx	Nx	M0	MSI-H	No	poorly differentiated		80	negative	No	Yes	Yes	No
GC050	pT2	pN0	M0	MSI-H	No	moderately differentiated		2	negative	No	Yes	Yes	No
GC051	pT1b	pN2	M0	Intestinal	No	poorly differentiated		5	negative	No	Yes	No	No
GC052	ypT3	ypN3	M0	Intestinal	Yes	NA		23	negative	No	Yes	No	No
GC053	pT4a	pN2	M0	Diffuse	Yes	poorly differentiated		0	negative	No	Yes	No	No
GC054	ypT2	ypN0	M0	Diffuse	No	poorly differentiated	2	10	negative	neoadj chemo	Yes	No	No
GC055	ypT4a	ypN3	M1	Diffuse	No	poorly differentiated		1	negative	No	Yes	No	No
GC056	ypT3	ypN1	M1	Intestinal	No	NA		10	negative	No	Yes	Yes	No
GC057	Tx	Nx	M0	MSI-H	No	moderately differentiated		0	negative	No	No	Yes	No
GC058	Tx	Nx	M1	NA	No	poorly differentiated		15	negative	No	No	No	No

GC059	ypT3	ypN0	M0	EBV	Yes	moderately to poorly differentiated		30	negative	No	Yes	Yes	No
GC060	ypT4b	ypN1	M0	Intestinal	No	NA		0	positive	neoadj chemo	Yes	No	Yes
GC061	Tx	Nx	M0	MSI-H	Yes	poorly differentiated		90	negative	No	No		No
GC062	ypT1a	ypN2	M0	Mixed	No	poorly differentiated		2	negative	No	Yes	No	No
GC063	ypT1b	ypN0	M0	Intestinal	Yes	moderately to poorly differentiated		70	negative	No	Yes	Yes	No
GC064	Tx	Nx	M0	MSI-H	No	moderately differentiated		30	negative	No	No		No

Tx, Nx pathological staging unknown; *NA* not available; *MSI-H* microsatellite instability high; *EBV* Epstein-Barr Virus associated; *TRG* tumor regression grade; *NP* not performed; *neoadj chemo* neoadjuvant chemotherapy; *chemo* chemotherapy; *immuno* immunotherapy

Extended Data Table 2: Patient demographics

Age	65.1 (11.0 - 90.0)
Stage	
Early	10 (15.6%)
Locally advanced	36 (56.2%)
Metastatic	18 (28.1%)
Gender	
Male	39 (60.9%)

Female	25 (39.1%)
Race	
White	44 (68.8%)
Asian	11 (17.2%)
Black	6 (9.4%)
NA	3 (4.7%)
Combined tumor subtype	
Intestinal	16 (25.0%)
Diffuse	13 (20.3%)
MSI-H	12 (18.8%)
Mixed	8 (12.5%)
EBV	3 (4.7%)
NA	12 (18.8%)
***H. pylori* history**	
No	47 (73.4%)
Yes	17 (26.6%)
T-stage	
ypT4b	2 (3.1%)
ypT4a	3 (4.7%)
ypT3	3 (4.7%)
ypT3	10 (15.6%)
ypT2	2 (3.1%)
ypT1b	3 (4.7%)
ypT1a	2 (3.1%)

ypT0	1 (1.6%)
pT4a	3 (4.7%)
pT3	2 (3.1%)
pT2	3 (4.7%)
pT1b	6 (9.4%)
pT1a	3 (4.7%)
NA	21 (32.8%)
N-stage	
ypN3	6 (9.4%)
ypN2	3 (4.7%)
ypN1	4 (6.2%)
ypN0	13 (20.3%)
pN2	4 (6.2%)
pN1	3 (4.7%)
pN0	10 (15.6%)
NA	21 (32.8%)
M-stage	
M1	18 (28.1%)
M0	42 (65.6%)
NA	4 (6.2%)
HER2 status	
Negative	57 (89.1%)
Positive	5 (7.8%)
NA	2 (3.1%)

PD-L1 CPS	
<1	18 (28.1%)
1-4	20 (31.2%)
5-9	4 (6.2%)
>=10	22 (34.4%)
Any Chemotherapy	
Yes	48 (75.0%)
No	16 (25.0%)
Any Immunotherapy	
No	41 (64.1%)
Yes	22 (34.4%)
NA	1 (1.6%)
Histological grade	
Well differentiated	1 (1.6%)
Moderately differentiated	17 (26.6%)
Moderately to poorly differentiated	7 (10.9%)
Poorly differentiated	38 (59.4%)
NA	1 (1.6%)

516 *NA* not available; *MSI-H* microsatellite instability high; *EBV* Epstein-Barr Virus associated

517 **Extended Data Table 3**: Data subsets and cell counts

Object	Cell count	Sample count	Gene count
Anndata object: all cell types	296,231	192	36601

Anndata QCed, cells with <200 genes and samples with <100 cells removed; doublets removed, cells with >40% mitochondrial genes removed). 13 samples removed due to failing QC/insufficient cell count.	251,167	179	36601
Subset to CD45+ cells. Cells with >10% mitochondrial genes removed. Cells double positive and double negative for CD4/CD8 removed.	152,981	179	36601

518 *Anndata* structed data format used in Scanpy eco-system; *QCed* after quality control

519 **Extended Data Table 4:** Top 50 DEGs for cell type cluster annotation for CD45+, CD8, CD4

520 and Myeloid subsets

521 (see attached file)

522 **Extended Data Table 5**: Patients with dLN and tumor IREA types

GC Patient ID	Collection	Lymph Node cytokine group	Tumor cytokine group
GC001		NaN	Tumor Immune Silent
GC002		LN Canonical	NaN
GC003	First collection	NaN	Tumor Inflamed Myeloid
GC003	Second collection	NaN	Tumor T Cell Engaged
GC004		NaN	NaN
GC005		NaN	Tumor T Cell Engaged
GC006		NaN	Tumor T Cell Engaged
GC007		NaN	Tumor Inflamed Myeloid
GC008		NaN	Tumor Inflamed Myeloid
GC009		LN Disrupted	Tumor Inflamed Myeloid
GC010		LN Disrupted	Tumor Immune Silent
GC011		LN Canonical	Tumor Inflamed Myeloid
GC012		NaN	Tumor T Cell Engaged
GC013	First collection	NaN	Tumor T Cell Engaged
GC013	Second collection	NaN	Tumor T Cell Engaged
GC014		LN Canonical	Tumor T Cell Engaged
GC015	First collection	NaN	Tumor T Cell Engaged
GC015	Second collection	LN Canonical	Tumor T Cell Engaged
GC016		LN Canonical	Tumor Immune Silent
GC017		NaN	Tumor T Cell Engaged
GC019		NaN	Tumor Immune Silent

GC020		NaN	Tumor Immune Silent
GC021	First collection	NaN	Tumor T Cell Engaged
GC021	Second collection	NaN	Tumor T Cell Engaged
GC022		LN Disrupted	Tumor Inflamed Myeloid
GC023		LN Disrupted	Tumor Immune Silent
GC024		LN Disrupted	Tumor Inflamed Myeloid
GC025		NaN	Tumor Inflamed Myeloid
GC026		NaN	Tumor T Cell Engaged
GC027		LN Canonical	Tumor Inflamed Myeloid
GC028	First collection	LN Disrupted	Tumor T Cell Engaged
GC028	Second collection	LN Canonical	Tumor T Cell Engaged
GC029		NaN	Tumor Inflamed Myeloid
GC030		LN Disrupted	Tumor Immune Silent
GC031		NaN	Tumor Immune Silent
GC032		NaN	Tumor T Cell Engaged
GC033		LN Disrupted	Tumor Inflamed Myeloid
GC034		LN Disrupted	Tumor Inflamed Myeloid
GC035		NaN	Tumor Immune Silent
GC036		LN Disrupted	Tumor T Cell Engaged
GC037		NaN	Tumor Immune Silent
GC038		LN Disrupted	Tumor T Cell Engaged
GC039		LN Disrupted	Tumor Immune Silent
GC040		LN Canonical	Tumor T Cell Engaged
GC041		LN Disrupted	Tumor Immune Silent
GC042		NaN	Tumor Immune Silent
GC043		NaN	Tumor Immune Silent
GC044		NaN	NaN
GC045		LN Disrupted	Tumor Immune Silent
GC046		NaN	Tumor Immune Silent
GC047	First collection	NaN	Tumor T Cell Engaged
GC047	Second collection	LN Canonical	NaN
GC048		NaN	Tumor T Cell Engaged
GC049		NaN	Tumor T Cell Engaged
GC050		LN Disrupted	Tumor Inflamed Myeloid
GC051		LN Canonical	Tumor T Cell Engaged
GC052	First collection	NaN	Tumor T Cell Engaged
GC052	Second collection	LN Canonical	Tumor T Cell Engaged

GC053		LN Disrupted	Tumor T Cell Engaged
GC054		LN Disrupted	Tumor Immune Silent
GC055	First collection	NaN	Tumor Immune Silent
GC055	Second collection	LN Disrupted	Tumor T Cell Engaged
GC056	First collection	NaN	Tumor Immune Silent
GC056	Second collection	LN Disrupted	Tumor Immune Silent
GC057		NaN	Tumor T Cell Engaged
GC058		LN Canonical	Tumor T Cell Engaged
GC059	First collection	NaN	Tumor T Cell Engaged
GC059	Second collection	LN Canonical	Tumor T Cell Engaged
GC060		LN Canonical	Tumor T Cell Engaged
GC061		NaN	Tumor T Cell Engaged
GC062	First collection	NaN	Tumor T Cell Engaged
GC062	Second collection	LN Disrupted	NaN
GC063	First collection	NaN	Tumor T Cell Engaged
GC063	Second collection	LN Canonical	Tumor Inflamed Myeloid
GC064		NaN	Tumor T Cell Engaged

LN lymph node; *NaN* IREA group not able to be calculated

END NOTES

Acknowledgements

This research was supported in part by the institution's Cancer Center Support Grant (P30 CA008748) from the NIH, and the Cycle for Survival-Equinox Grant (MA, EES, VES, SAV). SAV was supported by a Damon Runyon Clinical Investigator Award. This work was additionally supported by research funding from Bristol Myers Squibb. Figure 1a was made using Biorender.com. We thank the MSKCC Single Cell Analysis and Innovation Lab (SAIL) for their thoughtful insights and assistance and Anthony Verdone for assistance with data management.

Author Contributions

EES, SS, SS, MA, HL, VES, SPS, and SAV conceived the project and designed all experiments. SS, MA, HD, VES and EES performed all sample acquisition. EES and SS assembled all metadata and reviewed clinical characteristics. YHL, SS and EES performed all tissue

537 processing. YHL and EES performed all spectral cytometry assays. YHL and EES performed all
538 laboratory experiments. SS, HL, MZ, and NC performed all computational and statistical
539 analyses. EES, SS, HL, SPS, VES and SAV wrote the manuscript; all authors reviewed the
540 manuscript.
541
542 **Competing Interests Statement**
543
544 VES has received speaking honoraria from Merck Pharmaceuticals and Astra Zeneca. SAV is
545 an advisor for Generate Bio and for the Institute for Follicular Lymphoma Innovation (I-FLI),
546 previously served as a consultant for Koch Disruptive Technologies and has received research
547 funding from Bristol Meyers Squibb. SPS reports grants/contracts from AstraZeneca and Bristol
548 Meyers Squibb and a leadership role in the Genome Canada Scientific Advisory Council. ML
549 ML is supported by a grant from the NIDDK of the NIH (K08 DK125876). No other authors have
550 relationships with outside entities to disclose.
551
552 **Data Availability**
553 Supplementary Information is available for this paper.
554 Data is available at ***.
555 Correspondence and requests for materials should be addressed to shahs3@mskcc.org,
556 strongv@mskcc.org, or vardhans@mskcc.org.
557 Reprints and permissions information is available at www.nature.com/reprints.
558
559

REFERENCES

1 *SEER*Explorer: An interactive website for SEER cancer statistics [Internet].* <https://seer.cancer.gov/statistics-network/explorer/> (2025 Apr 16).

2 Schistosomes, liver flukes and Helicobacter pylori. *IARC Monogr Eval Carcinog Risks Hum* **61**, 1-241 (1994).

3 Fu, K. *et al.* Streptococcus anginosus promotes gastric inflammation, atrophy, and tumorigenesis in mice. *Cell* **187**, 882-896 e817 (2024). https://doi.org/10.1016/j.cell.2024.01.004

4 Norcross, J. W., Monroe, S. E. & Griffin, B. G. The development of gastric carcinoma in pernicious anemia. *Ann Intern Med* **37**, 338-343 (1952). https://doi.org/10.7326/0003-4819-37-2-338

5 Sasaki, H. *et al.* Presence of Streptococcus anginosus DNA in esophageal cancer, dysplasia of esophagus, and gastric cancer. *Cancer Res* **58**, 2991-2995 (1998).

6 Zamcheck, N., Grable, E., Ley, A. & Norman, L. Occurrence of gastric cancer among patients with pernicious anemia at the Boston City Hospital. *N Engl J Med* **252**, 1103-1110 (1955). https://doi.org/10.1056/NEJM195506302522601

7 Rooney, M. S., Shukla, S. A., Wu, C. J., Getz, G. & Hacohen, N. Molecular and genetic properties of tumors associated with local immune cytolytic activity. *Cell* **160**, 48-61 (2015). https://doi.org/10.1016/j.cell.2014.12.033

8 Abate, M. *et al.* Host Tissue Factors Predict Immune Surveillance and Therapeutic Outcomes in Gastric Cancer. *Cancer Immunol Res* **13**, 591-601 (2025). https://doi.org/10.1158/2326-6066.CIR-23-0563

9 Stoeckius, M. *et al.* Simultaneous epitope and transcriptome measurement in single cells. *Nat Methods* **14**, 865-868 (2017). https://doi.org/10.1038/nmeth.4380

10 Lauren, P. The Two Histological Main Types of Gastric Carcinoma: Diffuse and So-Called Intestinal-Type Carcinoma. An Attempt at a Histo-Clinical Classification. *Acta Pathol Microbiol Scand* **64**, 31-49 (1965). https://doi.org/10.1111/apm.1965.64.1.31

11 Cancer Genome Atlas Research, N. Comprehensive molecular characterization of gastric adenocarcinoma. *Nature* **513**, 202-209 (2014). https://doi.org/10.1038/nature13480

12 Bellmunt, J. *et al.* Pembrolizumab as Second-Line Therapy for Advanced Urothelial Carcinoma. *N Engl J Med* **376**, 1015-1026 (2017). https://doi.org/10.1056/NEJMoa1613683

13 Pai, J. A. & Satpathy, A. T. High-throughput and single-cell T cell receptor sequencing technologies. *Nat Methods* **18**, 881-892 (2021). https://doi.org/10.1038/s41592-021-01201-8

14 Cui, A. *et al.* Dictionary of immune responses to cytokines at single-cell resolution. *Nature* **625**, 377-384 (2024). https://doi.org/10.1038/s41586-023-06816-9

15 Jin, S. *et al.* Inference and analysis of cell-cell communication using CellChat. *Nat Commun* **12**, 1088 (2021). https://doi.org/10.1038/s41467-021-21246-9

16 Jin, S., Plikus, M. V. & Nie, Q. CellChat for systematic analysis of cell-cell communication from single-cell transcriptomics. *Nat Protoc* **20**, 180-219 (2025). https://doi.org/10.1038/s41596-024-01045-4

17 Nakauchi, M. *et al.* Outcomes of Neoadjuvant Chemotherapy for Clinical Stages 2 and 3 Gastric Cancer Patients: Analysis of Timing and Site of Recurrence. *Ann Surg Oncol* **28**, 4829-4838 (2021). https://doi.org/10.1245/s10434-021-09624-5

605 18 Akbar, A. N., Terry, L., Timms, A., Beverley, P. C. & Janossy, G. Loss of CD45R and gain
606 of UCHL1 reactivity is a feature of primed T cells. *J Immunol* **140**, 2171-2178 (1988).
607 19 Serra, H. M., Krowka, J. F., Ledbetter, J. A. & Pilarski, L. M. Loss of CD45R (Lp220)
608 represents a post-thymic T cell differentiation event. *J Immunol* **140**, 1435-1441 (1988).
609 20 Tedder, T. F., Penta, A. C., Levine, H. B. & Freedman, A. S. Expression of the human
610 leukocyte adhesion molecule, LAM1. Identity with the TQ1 and Leu-8 differentiation
611 antigens. *J Immunol* **144**, 532-540 (1990).
612 21 Telerman, A. *et al.* Internalization of human T lymphocyte receptors. *Eur J Immunol* **17**,
613 991-997 (1987). https://doi.org/10.1002/eji.1830170715
614 22 Miyawaki, T. *et al.* Differential expression of apoptosis-related Fas antigen on lymphocyte
615 subpopulations in human peripheral blood. *J Immunol* **149**, 3753-3758 (1992).
616 23 Kuo, C. T., Veselits, M. L. & Leiden, J. M. LKLF: A transcriptional regulator of single-
617 positive T cell quiescence and survival. *Science* **277**, 1986-1990 (1997).
618 https://doi.org/10.1126/science.277.5334.1986
619 24 Mimitou, E. P. *et al.* Scalable, multimodal profiling of chromatin accessibility, gene
620 expression and protein levels in single cells. *Nat Biotechnol* **39**, 1246-1258 (2021).
621 https://doi.org/10.1038/s41587-021-00927-2
622 25 Schober, S. L. *et al.* Expression of the transcription factor lung Kruppel-like factor is
623 regulated by cytokines and correlates with survival of memory T cells in vitro and in vivo.
624 *J Immunol* **163**, 3662-3667 (1999).
625 26 Schep, A. N., Wu, B., Buenrostro, J. D. & Greenleaf, W. J. chromVAR: inferring
626 transcription-factor-associated accessibility from single-cell epigenomic data. *Nat*
627 *Methods* **14**, 975-978 (2017). https://doi.org/10.1038/nmeth.4401
628 27 Liu, J. *et al.* CTCF mediates CD8+ effector differentiation through dynamic redistribution
629 and genomic reorganization. *J Exp Med* **220** (2023).
630 https://doi.org/10.1084/jem.20221288
631 28 Raczkowski, F. *et al.* The transcription factor Interferon Regulatory Factor 4 is required for
632 the generation of protective effector CD8+ T cells. *Proc Natl Acad Sci U S A* **110**, 15019-
633 15024 (2013). https://doi.org/10.1073/pnas.1309378110
634 29 Yao, S. *et al.* Interferon regulatory factor 4 sustains CD8(+) T cell expansion and effector
635 differentiation. *Immunity* **39**, 833-845 (2013).
636 https://doi.org/10.1016/j.immuni.2013.10.007
637 30 Man, K. *et al.* Transcription Factor IRF4 Promotes CD8(+) T Cell Exhaustion and Limits
638 the Development of Memory-like T Cells during Chronic Infection. *Immunity* **47**, 1129-
639 1141 e1125 (2017). https://doi.org/10.1016/j.immuni.2017.11.021
640 31 Harberts, A. *et al.* Interferon regulatory factor 4 controls effector functions of CD8(+)
641 memory T cells. *Proc Natl Acad Sci U S A* **118** (2021).
642 https://doi.org/10.1073/pnas.2014553118
643 32 Miyagawa, F. *et al.* Interferon regulatory factor 8 integrates T-cell receptor and cytokine-
644 signaling pathways and drives effector differentiation of CD8 T cells. *Proc Natl Acad Sci*
645 *U S A* **109**, 12123-12128 (2012). https://doi.org/10.1073/pnas.1201453109
646 33 Miller, I. J. & Bieker, J. J. A novel, erythroid cell-specific murine transcription factor that
647 binds to the CACCC element and is related to the Kruppel family of nuclear proteins. *Mol*
648 *Cell Biol* **13**, 2776-2786 (1993). https://doi.org/10.1128/mcb.13.5.2776-2786.1993
649 34 Schultess, J., Danielewski, O. & Smolenski, A. P. Rap1GAP2 is a new GTPase-activating
650 protein of Rap1 expressed in human platelets. *Blood* **105**, 3185-3192 (2005).
651 https://doi.org/10.1182/blood-2004-09-3605

652 35 Molina-Ortiz, P. *et al.* Rasa3 controls megakaryocyte Rap1 activation, integrin signaling
653 and differentiation into proplatelet. *PLoS Genet* **10**, e1004420 (2014).
654 https://doi.org/10.1371/journal.pgen.1004420
655 36 Stefanini, L. *et al.* RASA3 is a critical inhibitor of RAP1-dependent platelet activation. *J*
656 *Clin Invest* **125**, 1419-1432 (2015). https://doi.org/10.1172/JCI77993
657 37 Wang, X. *et al.* A phase II study of a modified FOLFOX6 regimen as neoadjuvant
658 chemotherapy for locally advanced gastric cancer. *Br J Cancer* **114**, 1326-1333 (2016).
659 https://doi.org/10.1038/bjc.2016.126
660 38 Man, S. M. Inflammasomes in the gastrointestinal tract: infection, cancer and gut
661 microbiota homeostasis. *Nat Rev Gastroenterol Hepatol* **15**, 721-737 (2018).
662 https://doi.org/10.1038/s41575-018-0054-1
663 39 Hussain, S. P., Hofseth, L. J. & Harris, C. C. Radical causes of cancer. *Nat Rev Cancer* **3**,
664 276-285 (2003). https://doi.org/10.1038/nrc1046
665 40 Good, R. A. Relations between immunity and malignancy. *Proc Natl Acad Sci U S A* **69**,
666 1026-1032 (1972). https://doi.org/10.1073/pnas.69.4.1026
667 41 Immunodeficiency disease and malignancy. Various immunologic deficiencies of man and
668 the role of immune processes in the control of malignant disease. *Ann Intern Med* **77**,
669 605-628 (1972).
670 42 Fagerberg, E. *et al.* KLF2 maintains lineage fidelity and suppresses CD8 T cell exhaustion
671 during acute LCMV infection. *Science* **387**, eadn2337 (2025).
672 https://doi.org/10.1126/science.adn2337
673 43 Shao, T. Y. *et al.* Kruppel-like factor 2+ CD4 T cells avert microbiota-induced intestinal
674 inflammation. *Cell Rep* **42**, 113323 (2023). https://doi.org/10.1016/j.celrep.2023.113323
675 44 Schwandt, T. *et al.* Expression of type I interferon by splenic macrophages suppresses
676 adaptive immunity during sepsis. *EMBO J* **31**, 201-213 (2012).
677 https://doi.org/10.1038/emboj.2011.380
678 45 Zehir, A. *et al.* Mutational landscape of metastatic cancer revealed from prospective
679 clinical sequencing of 10,000 patients. *Nat Med* **23**, 703-713 (2017).
680 https://doi.org/10.1038/nm.4333

681

1

METHODS

Patient Inclusion

Under Institutional Review Board approval (IRB 20-025) fresh tissue was collected from gastric tumors, distant normal gastric mucosa, draining gastric lymph nodes (dLN), and metastases from patients with gastric adenocarcinoma at Memorial Sloan Kettering Cancer Center (MSK). Patients had either institutional 6-107 and/or 12-245 tissue consent or specific IRB approval for tissue use after patient death. IRB approval was obtained for patients under 18. Tissues were collected from patients undergoing either gastric resection or diagnostic laparoscopy (DL) with esophagogastroduodenoscopy (EGD) as part of treatment or staging/diagnosis. Gastric resections were either open or robotic assisted. Biopsies taken during EGD were removed using cold endoscopic forceps, and biopsies taken during DL were removed using cold laparoscopic graspers. Pathology was reviewed by institutional gastrointestinal pathologists and all tumors were pathologically confirmed to be gastric adenocarcinoma. The 8th edition of the AJCC staging system was used by convention for pathologic TNM staging.[1] Clinical information for patients was collected prospectively in a clinical gastric database. Lauren classification[2] and TCGA classifications[3] were combined to describe patients with intestinal, diffuse, mixed, MSI-H and EBV tumors. MSI-H or EBV designation superseded Lauren classification. Lauren classification was determined by pathology report. MSI-H status was determined by immunohistochemistry (IHC) of MLH1, MSH2, MSH6, and PMS2 as reported by pathology or by tumor mutation burden on institutional genomic testing (MSK IMPACT). EBV positivity was determined by IHC on pathology report. HER2 status was reported as negative, positive, or NA (not available) as a summary of HER2 IHC and fluorescence in situ hybridization (FISH) analysis for equivocal IHC results from pathology reports. PD-L1 scores were reported as CPS from 0-100, with any scores over 100 reduced to 100. For patients who received systemic therapy prior to resection, tumor response grade (TRG) was reported as called in the institutional pathology report from 0-3

28 according to the NCCN system.[4] *H. pylori* history was determined by a previous positive IHC
29 test or a documentation of previous *H. pylori* infection or treatment in a patient's chart.
30 Treatments were grouped as chemotherapy, immunotherapy, trastuzumab, radiation, or other
31 and were categorized as prior to or following specimen collection. Survival, follow-up, and
32 recurrence were collected up to January 17, 2025. Outcomes for two patients were not included
33 due to their enrollment in a clinical trial after specimen collection. Disaggregated data could not
34 be publicly shared for **7** patients due to IRB restrictions.
35
36 **Sample Collection and Processing**
37
38 As mentioned above, tissue was collected in the operating room from clinically indicated gastric
39 cancer resections or DLs with EGDs. During robotic gastric resections, Indocyanin Green (ICG)
40 was injected intra-operatively to mark the tumor bed and highlight tumor-draining lymph nodes
41 as previously described.[5] During open operations, tumor draining lymph nodes were determined
42 by the operating surgeon according to tumor location and lymph node station. For gastrectomies,
43 within 3 minutes of resection, 0.5-1.0 cm^3 of tumor, distant normal gastric mucosa (defined as
44 macroscopically normal appearing to the surgeon and not directly adjacent to the tumor), and
45 LNs (identified to be draining nodes by ICG or station by operating surgeon) were isolated, cut
46 into ~1 mm^3 pieces and placed into 15mL conical tubes containing phosphate buffered saline
47 (PBS). These samples were placed on ice and immediately transported to the laboratory. During
48 DL with EGD tumor and distant normal samples were collected during EGD with endoscopic
49 cold forceps, 4 bites of tumor were collected then immediately suspended in PBS, as were 3
50 bites of distant normal gastric mucosa with the forceps cleaned in-between collections. If
51 peritoneal or liver metastases were seen on DL with sufficient tissue for pathologic diagnosis, a
52 biopsy of 0.5 cm^3 of metastasis was collected and immediately transferred to a 15mL conical

53 tube with PBS. These samples were placed on ice and immediately transported to the laboratory
54 in the same manner as for gastric resections. All samples were digested using a GentleMACS
55 Dissociator in 2.2 ml or 4.7mL (based on tissue size) of R-10 solution (RPMI, 10% fetal bovine
56 serum, 10mM HEPES, 1% penicillin-streptomycin, 1% L-glutamine) and Miltenyi enzymes
57 (Miltenyi Biotec Tumor Dissociation Kit, Human) at 37ºC using GentleMACS program TK3. The
58 digested tissue was then filtered through a 100-µm cell strainer and washed with cold R-10.
59 Samples were centrifuged at 500 *g* x 5 minutes at 4°C and supernatant was aspirated. Pelleted
60 cells were resuspended in 1mL of ammonium-chloride-potassium (ACK) lysing buffer for 3
61 minutes at room temperature and then washed with 5 mL of R-10. Samples were centrifuged
62 again at 500 *g* x 5 minutes at 4°C and supernatant was aspirated, the cell pellet was
63 resuspended in 1mL of RPMI plus 2uL of 20mg/mL DNase and incubated at room temperature
64 for 5 minutes. After incubation 4mL of R10 was added and cells were counted. Cells were spun
65 again at 500 *g* x 5 minutes at 4°C and resuspended in 1 million/mL aliquots in BAMBANKER
66 Serum-Free Cell Freezing Medium (Wako Chemicals) for cryopreservation at -80°C.
67

68 **Single cell immune profiling**

69

70 Samples were batched for multiplexed combined 3' single-cell RNA, 5' T-cell receptor (TCR),
71 and cell-surface epitope assessment (CITE-seq) (10x Genomics.) Selected samples were
72 thawed from -80°C in a 37°C water bath with gentle agitation, transferred to a 15mL conical tube
73 and then slowly diluted with 9mL of RPMI. Samples were then centrifuged at 200 rpm for 10 min
74 at 4°C and the supernatant was aspirated. Each sample was resuspended in 50uL of 1:400
75 dilution in PBS of Ghost Dye 510 (Tonbo) and transferred to a 96-well V-bottom plate, then
76 incubated at room temperature in the dark for 10 minutes. Samples were washed with 100uL of
77 PBS, centrifuged at 700*g* for 2 minutes at 4°C, and supernatant was discarded. Each sample

78 was then resuspended in 25 uL of Human TruStain FcX (Biolegand) diluted 1:20 in PBS and
79 incubated for 10 minutes in the dark on ice. Then an antibody pool of TotalSeq-C Human
80 Universal Cocktail V1.0 (Biolegend), TotalSeqC anti-human Hashtag Antibodies (Biolegend)
81 was added, and samples were incubated for 30 minutes on ice. Samples were washed with
82 100uL of PBS, centrifuged at 700*g* for 2 minutes at 4°C and supernatant was discarded. Cells
83 were then resuspended in 200uL of 0.5% bovine serum albumin (BSA) in PBS and transferred
84 to a flow tube with strainer cap. Cells were flow sorted for live cells and then pooled and counted.
85 All samples were concentrated to a volume of 50uL and then delivered to the Single Cell
86 Analytics Innovation Lab (SAIL) for library construction and sequencing.
87
88 Single-cell RNA-Seq of FACS-sorted cell suspensions was performed on Chromium instrument
89 (10x genomics) following the user manual for 5′ v2 chemistry. In brief, FACS-sorted cells were
90 washed once with PBS containing 2% bovine serum albumin (BSA) and resuspended in PBS
91 containing 2% BSA to a final concentration of 700–1,200 cells per µL. The viability of cells was
92 usually above 70%, as confirmed with 0.2% (w/v) Trypan Blue staining (Countess II). Between
93 10,000 and 30,000 cells were targeted for each sample, where several samples were
94 multiplexed together on one lane of 10x Chromium and specific extracellular protein epitope
95 characterized (using Antibody Derived Tag - ADT) according to the cell hashing protocol.[6]
96
97 The scRNA-seq and scTCR-seq libraries were prepared using the 10x Single Cell Immune
98 Profiling Solution Kit, according to the manufacturer's instructions. Briefly, amplified cDNA was
99 used for both 5′ gene expression library construction and TCR enrichment. For gene expression
100 library construction, amplified cDNA was fragmented and end-repaired, double-sided size-
101 selected with SPRIselect beads, PCR-amplified with sample indexing primers (98 °C for 45 s;
102 14–16 cycles of 98 °C for 20 s, 54 °C for 30 s, 72 °C for 20 s; 72 °C for 1 min), and double-sided
103 size-selected with SPRIselect beads.

104 For TCR library construction, TCR transcripts were enriched from 2 µl of amplified cDNA by PCR
105 (primer sets 1 and 2: 98 °C for 45 s; 10 cycles of 98 °C for 20 s, 67 °C for 30 s, 72 °C for 1 min;
106 72 °C for 1 min). Following TCR enrichment, enriched PCR product was fragmented and end-
107 repaired, size-selected with SPRIselect beads, PCR-amplified with sample-indexing primers
108 (98 °C for 45 s; 9 cycles of 98 °C for 20 s, 54 °C for 30 s, 72 °C for 20 s; 72 °C for 1 min), and
109 size-selected with SPRIselect beads.
110
111 Final libraries (GEX, TCR and HTO/CITE) were sequenced on Illumina NovaSeq S4 or X+
112 platform (R1 – 26 cycles, i7 – 10 cycles, i5 – 10 cycles, R2 – 90 cycles).
113
114 **Demultiplexing**
115 HTO sequencing data were aligned to the HTO barcodes, and UMIs were counted for each cell
116 using CITE-seq-Count. Using a two-component K-means algorithm, we partitioned logged HTO
117 counts into two distributions: background noise (lower mean) and positive tags (larger mean).
118 Each droplet was then assigned to its source sample based on tags in the positive signal
119 component. We classified droplets with multiple assignments as doublets and those with a single
120 assignment as singlets. This analysis was performed using SHARP v0.1.1
121 (https://github.com/hisplan/sharp).
122
123 **Single-Cell Analysis**
124 We used a hierarchical supervised approach to assign phenotypes to cells as follows. After QC
125 and pre-processing, we used unsupervised graph-based clustering to define the main CD45+
126 cell types. This yielded 6 separate clusters, namely T/NK, B, Plasma, Mast, Myeloid, and
127 Plasmacytoid DC (Figure 2a), annotated using known marker genes (Extended Fig. 1,
128 Supplementary Table 4).
129

130 **Preprocessing**

131 Raw binary base call (BCL) files were demultiplexed into FASTQ files using Cell Ranger. Gene
132 expression libraries were aligned to the GRCh38 reference genome and quantified using
133 `cellranger count` (v7.1.0). TCR V(D)J libraries were processed with `cellranger vdj`
134 (v6.1.2). Cell barcodes were selected using Cell Ranger's cell-calling algorithm EmptyDrops,
135 and the resulting whitelist was used to filter ADT data. The ADT data was then quantified using
136 the SHARP pipeline, which builds on CITE-seq-Count to count cell barcodes and UMIs. Finally,
137 these matrices—gene expression, ADT, and TCR—were loaded into individual AnnData objects
138 for downstream single-cell analysis.

139 Cells with fewer than 200 genes and more than 40% mitochondrial content were removed and
140 samples with fewer than 100 cells were removed. Doublet cells were identified using
141 scDblFinder[7] and excluded. Raw counts were normalized by library size and log-transformed
142 with a pseudo-count of 1 using Scanpy.[8] The top 2000 highly variable genes were selected
143 following the removal of ribosomal, mitochondrial and T cell receptor genes using the
144 `highly_variable_genes` function with the `flavor` option set to `seurat` and sample as
145 `batch_key`. Principal component analysis (PCA) was performed retaining the top 50 PCs.
146 `Harmonypy`[9] (v0.0.9) was used to perform batch correction to control for inter-patient variation.
147 The batch corrected embeddings were used for leiden clustering and creating the UMAP[10]
148 projection for visualization. Clusters for the broad cell lineages were annotated using marker
149 genes, derived from Wilcoxon rank-sum tests comparing each cluster to all others. The 8
150 annotated clusters were: B (MS4A1, CD19, CD79A), T/NK (CD3D, CD3E, NCAM1), epithelial
151 (EPCAM, KRT19, KRT8), endothelial (PECAM1, VWF, CDH5), fibroblasts (COL1A1, FAP,
152 PDGFRA), myeloid (CD14, LYZ, CSF1R), mast (KIT, TPSB2, FCER1A, CPA3, HDC, MS4A2),
153 and plasma (MZB1, SDC1, JCHAIN). Using these annotated cell type clusters, the data were
154 subset to CD45+ cells and cells with more than 10% mitochondrial content were removed. Highly

155 variable gene selection, PCA, batch correction, leiden clustering and UMAP computation were
156 performed as outlined above.
157
158 **Cell-type annotations**
159 CD45+ cells were annotated using a combination of gene expression and protein marker
160 intensity. Cells were grouped into major compartments, namely T/NK, myeloid, B, plasma, mast
161 and plasmacytoid DC cells (Supplementary Table 4). T cells were annotated using cite-seq
162 protein CD3D, with custom intensity thresholds to filter for CD4+ and CD8+ T cells using CD8A
163 and CD4 proteins, respectively. For CD4, CD8 and myeloid cells, clustering analysis was
164 performed and the UMAP re-computed for each subset. Differentially expressed genes between
165 clusters were evaluated alongside protein expression (e.g. CD45RA and CD45RO) to annotate
166 13 CD8, 11 CD4 and 7 myeloid subclusters (Supplementary Table 4).
167
168 **Gaussian Kernel Density Estimates**
169 We estimated cell density across the UMAP embedding using Scanpy's
170 `sc.tl.embedding_density` with default parameters, grouping cells by the respective
171 covariate. For each group, we visualized the resulting Gaussian kernel density using
172 `sc.pl.embedding_density`.
173
174 **Tensor factorization for Cytokine Activation using IREA**
175 We applied cytokine networks to identify intercellular cytokine driven bridging tumors and
176 tumor-draining lymph nodes. To do so, we computed an enrichment score for each of the 86
177 cytokines in each cell type per sample. To account for the variation of cell types and cytokines
178 in our samples, we used a Bayesian Poisson tensor factorization algorithm shown to be robust
179 to sparse datasets. The algorithm infers sample specific representations in terms of latent

factors. For each anatomical site of origin, we grouped samples based on their factor activation scores, using a nearest-neighbor graph community detection algorithm.

Concretely, top up-regulated genes in each cell type for each cytokine was acquired from a recently published cytokine dictionary (hereafter called IREA genes.)[11] For each sample, and each cytokine, the overlap between the IREA genes and the DE genes in each cell type was used to compute an overrepresentation analysis and p-values were computed via the hypergeometric test and corrected for multiple testing using false discovery rate (FDR). An enrichment score was computed as the negative log10 of the adjusted p-values per (sample, cell-type, cytokine) tuple. A sample by cytokine score was computed as the sum of all cytokine-cell type interactions. The sample by cell type by cytokine enrichment score, computed thus, was used as the input to the tensor factorization algorithm. Let x_{ijc}denote the enrichment of cytokine c , in cell type j , in sample i , then we assume the following decomposition: $x_{ijc} \approx \widehat{x_{ijc}} = \sum_{k=1}^{K} A_{ik}\, B_{jk} C_{ck}$ where $A \in R_{+}^{N \times K}$, $B \in R_{+}^{J \times K}$, $C \in R_{+}^{D \times K}$ are latent non-negative matrices, representing sample by factor, cell type by factor, and cytokine by factor scores respectively. To encourage sparsity, we use a Poisson likelihood $x_{ijc} \sim \text{Poisson}\left(x_{ijc}; \widehat{x_{ijc}}\right)$. The target of inference is the posterior distribution on the latent matrices A , B , C , that is, $P(A, B, C \mid X, \lambda)$. We use variational inference to infer the latent variables.

Cell type-Cytokine Activation Graph Construction

Let ψ_{ij} denote the activity of cytokine i in cell type j . We use $\psi \in R_{+}^{J \times C}$as a weighted adjacency matrix for a bipartite graph where nodes are the set of cytokines and cell types, and edges denote the inferred activity level of a source cytokine in a receiver cell type. To compute ψ, we average over factors to compute sample-specific (Cell-Type, Cytokine) pairings. For each sample, per Cell Type per Cytokine $\psi_{ij} = \sum_{k=1}^{K} A_{ik}\, B_{jk} C_{:K} \in R^{M}$. For each group of samples G , we can compute a cell type-cytokine activation matrix as $\psi_{Gj} \coloneqq \sum_{i \in G} \psi_{ij}$. Similarly, for a set of

204 cytokines H , we report a summary ψ_{GH} as $\psi_{GH} \coloneqq \sum_{i \in G, j \in H} \psi_{ij}$.

205

206 **Cytokine type groupings**

207 We grouped into biologically relevant cytokine families as below:

208 - Class 2 cytokines: IL-10 and all the interferons (k, g, e, b, a1)
209 - Common beta-chain cytokines: IL3, IL5, GM-CSF
210 - Colony stimulating factors: G-CSF, M-CSF, Flt3l
211 - Hormones: Prolactin, Adiponectin
212 - IL-1/Alarmin family: TSLP, IL1a, Il1b, IL18, IL33, IL36a
213 - IL-12 family: IL12, IL23, IL27
214 - IL-17 family: IL17E
215 - IL-2 family: IL2, IL7, IL15, IL21
216 - IL-6 family: IL11, IL31, LIF, Cardiotrophin, Neuropoietin, Oncostatin M
217 - Th2-like: IL4, IL9, IL13
218 - TNF family: TNF, TL1A, CD40L, BAFF

219

220 **Clustering of samples based on IREA scores**

221 We grouped samples that belong to each anatomical site separately. Briefly, given the sample
222 by factor matrix A , we selected rows corresponding to samples from the dLN (tumor), formed
223 the nearest neighbor graph and computed the leiden clustering with resolution 0.5. For tumor
224 samples, this initially yielded 4 clusters. For interpretability, we merged the two that were high in
225 T cell interactions.

226

227 **Receptor Ligand activation analysis**

228 We inferred cell-cell interactions using Cellchat,[12] calculating communication probabilities for
229 each cell type pair and associated significance using permutation testing for disrupted and
230 canonical lymph node samples separately. We merged these Cellchat objects to perform
231 comparisons between the two groups and to identify significantly differing ligand-receptor
232 interaction probabilities. We then filtered these results to cytokine interactions. To further
233 evaluate the evidence for these predicted interactions, we compared the gene expression for
234 each significant ligand or receptor highlighted by Cellchat. This was performed by pooling all
235 cells from each lymph node group and comparing gene expression using a Wilcoxon rank-sum
236 test with Benjamini–Hochberg correction for multiple comparisons. This strategy allowed us to
237 include all samples (particularly valuable for myeloid cell types due to the relatively low cell
238 counts for this cell lineage). Gene expression after pseudobulking by sample was assessed and
239 only genes that showed a consistent trend between the pseudobulked and pooled data were
240 retained in our results.
241
242 **CD8+ T cell Trajectory Analysis**
243 For trajectory analysis, we used Palantir and CellRank. First, we selected CD8+ T cells derived
244 from dLN and tumor samples based on prior annotations. We then identified the top 2,000 highly
245 variable genes using the Scanpy function `sc.pp.highly_variable_genes`. Next, we
246 computed the top 50 principal components using `sc.tl.pca` and performed batch correction
247 via Harmony integration across individual patient identifiers using
248 `sc.external.pp.harmony_integrate`. We computed a diffusion map based on these
249 Harmony-corrected PCA embeddings using `sc.tl.diffmap` to capture global structure and
250 lineage relationships. We initialized the pseudotime trajectory by selecting a root cell
251 representative of a biologically meaningful starting point—specifically, a cluster of phenotypically
252 naïve T cells identified using our annotations. We then used Palantir's

253 `palantir.core.run_palantir` function to infer cell fate potential and generate pseudotime
254 values, employing 1,000 waypoints. Finally, we use CellRank's
255 `cellrank.tl.terminal_states` and `cellrank.tl.lineages` functions, leveraging
256 Palantir-derived pseudotime and diffusion-based transition probabilities to identify terminal
257 states and major cellular lineages. We executed CellRank with 1,000 permutations to identify
258 lineage drivers and associated genes.
259

260 **Phenotype entropy**

261 We first compute the fraction of CD8+ T cells per sample. We then compute the Shannon entropy
262 as $H = \sum_{k=1}^{K} p_k \log(p_k)$.
263

264 **Identifying Naïve-cell subpopulations**

265 We used Gaussian Mixture Models (GMM) to identify subpopulations of naïve cells based on
266 the protein expression of CD45 isoforms. Briefly, we selected all cells that had a naïve phenotype
267 based on their transcription profile. We used Bayesian information criterion to select the number
268 of components for the GMM. We used the from `sklearn.mixture.GaussianMixture` with
269 a full covariance, `max_iter=10000`, and 100 random restarts.
270

271 **Distance between T Cell Phenotypes**

272 To compute the distance between different T cell phenotype clusters, we used the geometric
273 median computed Weiszfeld's algorithm.[13] Geometric median of a set of n points $\{X_i\}$, is defined
274 as the point y that minimizes the sum of distances from all points in the set, i.e., $y \coloneqq$
275 $\text{argmin}_{y \in R^D} \sum_{i=1}^{n} D(X_i - y)$, where D is the L_2 norm (Euclidean distance). We used the
276 diffusion map representation of cells as input. We computed the geometric median for each

277 phenotype group the computed the pairwise distance of geometric medians of each phenotype
278 cluster from all others.
279
280 **Tumor vs dLN Transcription Factor Comparison**
281 To find which transcription factors (TF) affect expansion in CD8+ T cells, we compared the
282 expression of TFs in CD8+ T cells, excluding the naïve phenotype, derived from Tumor to
283 draining lymph node. We obtained a list of human TFs[14] and ranked their expression using the
284 Wilcoxon rank-sum test.
285
286 **KLF2 Correlated Genes**
287 We used regularized linear regression to find genes predictive of KLF2's expression in a sample
288 specific manner. Gene expression counts were normalized for library-size, log-transformed, and
289 standardized such that the mean and the variance of each gene are zero and one respectively.
290 Using linear regression with an L2 penalty (i.e., ridge regression), we estimated a per sample
291 coefficient vector of per gene association with KLF2 expression. We used the collection of these
292 coefficients to compute a mean coefficient and Z-score per gene.
293
294 **KLF2 Gene Cloning**
295 The plasmid PpyCAG-KLF2-IB[15] was a gift from Austin Smith (Addgene plasmid # 60441;
296 http://n2t.net/addgene:60441; RRID:Addgene 60441), which contained human *KLF2*. PCR
297 amplification of *KLF2* was performed, using primers (in table below) and Q5® High-Fidelity DNA
298 Polymerase (New England Biolabs) according to manufacturer's instructions. A restriction digest
299 was performed of both source plasmid PpyCAG-KLF2-IB and destination plasmid pTRIP-SFFV-
300 mTagBFP-P2A (Addgene 102585), using BamHI-HF (New England Biolabs) and SalI-HF (New
301 England Biolabs) with rCutSmart™ Buffer (New England Biolabs) according to manufacturer's
302 instructions, gel isolated and purified. Construct assembly was then performed using Gibson

303 Assembly® Master Mix (New England Biolabs) according to manufacturer's instructions. The
304 constructed plasmid was then transformed into NEB 5-alpha competent *E. coli* cells (New
305 England Biolabs) using 1uL of plasmid DNA. Mini-prep using Qiagen Mini Kit (Qiagen) was
306 performed for 3 individual clones per manufacturer's instructions, and then Sanger sequencing
307 was used to confirm the appropriate sequence for clone 2 which was subsequently used for all
308 experiments.

309

310 **Cloning primer sequences**

Primer Experiment	**Primer Name**	**Primer Sequence**
KLF2 Overexpression Plasmid Primers	NL65_KLF2.F	gagaaccctggacctgcgatggcgctgagtgaacccatcc
	NL65_KLF2.R	cgaggtcgacactagtgctacatgtgccgtttcatgtgc
KLF2 Plasmid Sequencing Primer	SFFV-mTagBFP-F	caaacgccaagaccacatatag

311

312

313 **KLF2 Overexpression**

314 Lentivirus was produced using 293T cells as follows: briefly, 293T cells were transiently co-
315 transfected with viral packaging (pCG-gag-pol), and envelope (pCG-VSVg) constructs along with
316 the expression vector (pTRIP-SFFV-mTagBFP-P2A-Empty or pTRIP-SFFV-mTagBFP-P2A-
317 KLF2) using 100 mg/mL polyethylenimine (Polysciences Inc). Virus-containing supernatant was
318 collected beginning 48 hours after transfection and filtered with a 0.45μm syringe, then aliquoted
319 and stored at -80°C until use. Primary human T-cell activation was performed as follows: Buffy
320 coats containing PBMCs were obtained from New York Blood Center. PBMCs were isolated

321 using Lymphoprep density gradient-based centrifugation. Subsequently, T cells were isolated
322 using a Dynabeads Untouched Human T Cell kit according to manufacturer's instructions. T cells
323 were activated in T cell media (RPMI-1640 supplemented with 10% heat-inactivated FBS, 2 mM
324 *L*-glutamine, and 100 U/mL Penicillin-Streptomycin) supplemented with recombinant IL-2
325 (Peprotech, 5 ng/mL). Cells were plated onto non-tissue culture-treated 6-well plates that had
326 been coated with anti-CD3 (Biolegend, 5 µg/mL) and anti-CD28 antibody (Biolegend, 2 µg/mL)
327 in PBS. 24 hours after activation, 100x concentrated virus was diluted 1:50 in T cell media (40uL
328 virus in 160uL T cell media, see above), then 200uL was added dropwise to each well and plates
329 were shaken gently. 24 hours later, cells were passaged into tissue culture-treated 6-well plates
330 containing fresh T cell media supplemented with IL-2. 5 days following initial stimulation, cells
331 were either harvested directly for spectral cytometry-based phenotyping, DOGMA-Seq,
332 assessment of KLF2 by Western blot, or restimulated to interrogate intracellular cytokine
333 production as described below.
334
335 **Protein extraction and Western Blot**
336 Cell lysis was performed using RIPA buffer (Cell Signaling) containing 1% SDS as well as
337 protease and phosphatase inhibitors. Following lysis, cells were sonicated (Bioruptor) and
338 centrifuged and supernatants were analyzed for protein concentration using BCA. 40 ug of each
339 lysate were run on a 4-12% Bis-Tris Gel (Thermo Fisher) and transferred to nitrocellulose
340 membranes. Membranes were blocked using 5% milk and then blotted with the following
341 antibodies: anti-KLF2 (see table below) and anti-H3 (see table below) in 3% BSA overnight at
342 4C on a rocker. Membranes were washed and then incubated with HRP-conjugated secondary
343 antibodies at 1:5000 dilution for 1 hour at room temperature in 5% milk. Membranes were then
344 washed and imaged using a Bio-Rad ChemiDoc Imaging System.
345

Target Name	Host	Company	Catalog #	Dilution
KLF2	Mouse	Novus Biologicals	NBP2-61812-0.025ml	1:1000
Histone H3	Rabbit	Cell Signaling	9715	1:1000
Anti-mouse IgG, HRP-linked Antibody	Horse	Cell Signaling	7076	1:5000
Amersham ECL Rabbit IgG, HRP-linked whole Ab	Donkey	Cytiva	NA934	1:5000

346

347 **Spectral Cytometry**

348 For phenotyping, cells were incubated with Fc block (Human TruStain FcX, Biolegend, cat.
349 422302) at a 1:20 dilution for 30 minutes at 4°C. Viability staining was performed for 30 minutes
350 at 4°C using Ghost Dye 510 Violet (cat. 59863) diluted 1:800 in PBS. Cells were subsequently
351 washed and stained for surface markers in FACS buffer containing 1X Brilliant Buffer (cat.
352 566349) for 30 minutes at 4°C, then washed twice and resuspended in 1% BSA in PBS. Data
353 was acquired using a Cytek Aurora spectral cytometer.

354

Staining type	Marker	Fluorophore	Catalog #	Clone	Dilution
Phenotype, Surface	PD-1	APC	BioLegend, 329908	EH12.2H7	1:100
	CCR7	BB700	BD Biosciences, 566437	3D12	1:50

	CD45RA	BUV395	BD Biosciences, 740298	HI100	1:400
	CD8	BUV496	BD Biosciences, 612943	RPA-T8	1:800
	CD38	BUV661	BD Biosciences, 612969	HIT2	1:200
	HLA-DR	BV786	BD Biosciences, 564041	G46-6	1:200
	CD4	BV570	BioLegend, 300534	RPA-T4	1:800
	CD28	BUV805	BD Biosciences, 742037	CD28.2 (RUO)	1:100
	CD69	BV605	BioLegend, 310937	FN50	1:200
	Tim-3	BV650	BioLegend, 345028	F38-2E2	1:50
	CD103	PE-594	BioLegend, 350223	Ber-ACT8	1:100
	CD39	PE-810	BioLegend, 328245	A1	1:100
	CXCR3	A700	BD Biosciences, 561320	1C6/CXCR3	1:100
	CXCR6	BV421	BioLegend, 356013	K041E5	1:100

Phenotype, Intracellular	TCF-1	A488	Cell Signaling, 6444S	C63D9	1:100
	TOX	PE	MACS Miltenyi Biotec, 130-120-716	REA473	1: 25
	CTLA4	BV711	BioLegend, 369632	BNI3	1: 200

355 For interrogation of cytokine production, PMA and ionomycin were added to wells to a final
356 concentration of 50 ng/mL and 500 ng/mL, respectively. 1 hour after addition of PMA and
357 ionomycin, Brefeldin A was added at a 1:1000 dilution and cells were incubated for another 3
358 hours, after which they were harvested and stained with surface antibodies as described above
359 using the panel below. Fixation was performed using an eBioscience FoxP3
360 Fixation/Permeabilization kit and stained overnight with intracellular antibodies diluted in
361 permeabilization buffer overnight at 4C. Data was acquired using a Cytek Aurora spectral
362 cytometer.

363

Staining type	**Marker**	**Fluorophore**	**Catalog #**	**Clone**	**Dilution**
Restimulation, Surface	PD-1	APC	BioLegend, 329908	EH12.2H7	1: 100
	CCR7	BB700	BD Biosciences, 566437	3D12	1: 50

	CD45RA	BUV395	BD Biosciences, 740298	HI100	1: 400
	CD8	BUV496	BD Biosciences, 612943	RPA-T8	1: 800
	CD38	BUV661	BD Biosciences, 612969	HIT2	1: 200
	HLA-DR	BV786	BD Biosciences, 564041	G46-6	1: 200
	CD4	BV570	BioLegend, 300534	RPA-T4	1: 800
	CD28	BUV805	BD Biosciences, 742037	CD28.2 (RUO)	1: 100
	CD69	BV605	BioLegend, 310937	FN50	1: 200
	Tim-3	BV650	BioLegend, 345028	F38-2E2	1: 50
	CD103	PE-594	BioLegend, 350223	Ber-ACT8	1: 100
	CD39	PE-810	BioLegend, 328245	A1	1: 100

Restimulation, Intracellular	GzmB	A700	BD Biosciences, 560213	GB11	1: 1600
	GzmK	FITC	BioLegend, 370508	GM26E7	1: 800
	IL-2	APC-F750	BioLegend, 500351	MQ1-17H12	1: 400
	IFN-g	BV421	BioLegend, 502531	4S.B3	1: 800
	TNF	PE	BioLegend, 502908	MAb11	1: 800

364

365 **DOGMA-Seq**

366 Primary human T cells were isolated and cultured as described above ('**KLF2 Overexpression**').
367 On day 5 following initial activation, T cells were collected and stained with a viability dye
368 followed by surface staining with anti-CD4 (RPA-T4, BioLegend 300534, 1:100), anti-CD8 (RPA-
369 T8, BD Biosciences 612914, 1:1200), TotalSeq-A Human Universal Cocktail, and TSA-
370 compatible hashtag oligos for multiplexing. Live BFP+ $CD4^+$ and $CD8^+$ T cells from both KLF2
371 overexpressing and empty vector conditions were flow sorted and delivered to SAIL for
372 sequencing. Single Cell Multiome ATAC + Gene Expression was performed with 10x genomics
373 system using Chromium Next GEM Single Cell Multiome Reagent Kit. We followed User Guide
374 with the difference that single cell suspension was prepared as described in Mimitou et al
375 (DOGMA-seq protocol with Digitonin buffer).[16] Around 10,000 cells were targeted for each
376 sample. Samples were multiplexed together on one lane of 10x Chromium (using Hash Tag
377 Oligonucleotides - HTO) and specific extracellular protein epitope characterized (using Antibody

378 Derived Tag - ADT) following previously published protocol.[6] Next, cells were treated with a
379 digitonin lysis buffer (20 mM Tris-HCl pH 7.4, 150 mM NaCl, 3 mM MgCl2, 0.01% DIG and 2 U
380 μl−1 of RNase inhibitor) for 5 min on ice, followed by adding 1 ml of chilled DIG wash buffer
381 (20 mM Tris-HCl pH 7.4, 150 mM NaCl, 3 mM MgCl2 and 1 U μl−1 of RNAse inhibitor) and
382 inversion before centrifugation at 500g for 5 min at 4 °C. The supernatant was discarded, and
383 cells were resuspended in DIG wash buffer, followed by counting using trypan blue and DAPI
384 on a Countess II FL Automated Cell Counter. Then cells were processed according to the
385 Chromium Next GEM Single Cell Multiome ATAC + Gene Expression user guide. Final libraries
386 were sequenced on Illumina NovaSeq X+ platform following 10x genomics recommendations.
387
388 For sample demultiplexing, HTO sequencing data were aligned to the HTO barcodes, and UMIs
389 were counted for each cell using CITE-seq-Count. Using a two-component K-means algorithm,
390 we partitioned logged HTO counts into two distributions: background noise (lower mean) and
391 positive tags (larger mean). Each droplet was then assigned to its source sample based on tags
392 in the positive signal component. We classified droplets with multiple assignments as doublets
393 and those with a single assignment as singlets. This analysis was performed using SHARP
394 v0.1.1 (https://github.com/hisplan/sharp).
395
396 **Cell typing of DOGMA-seq**

397 The KLF2 over-expression and empty vector were demultiplexed as above in '**DOGMA-Seq**'.
398 We processed single-cell RNA-, ATAC- and CITE-seq (DOGMA-seq) data using the Seurat (v.
399 5.0.3) and Signac packages (v.1.13.0). A total of 9,616 cells were sequenced, 6,487 in the KLF2
400 over-expression and 3,129 in the empty vector conditions. We loaded RNA and ATAC-seq data
401 into a single Seurat object. We computed quality control metrics—including nucleosome signal
402 and transcription start site (TSS) enrichment and filtered cells based on RNA/ATAC count

403 thresholds, nucleosome signal, and TSS enrichment to exclude low-quality cells. Next, we
404 established a unified peak set by merging and filtering called peaks, removing non-standard
405 chromosomes and blacklist regions. We quantified ATAC counts within these peaks using
406 `FeatureMatrix` and added them to a new chromatin assay in the Seurat object. We then split
407 the CD4+ and CD8+ T cells based on the CD4 and CD8A protein expression. To annotate cell
408 phenotypes, we normalized the RNA expression counts with `SCTransform` and reduced
409 dimensions using `RunPCA`. We processed ATAC data with term frequency-inverse document
410 frequency (`RunTFIDF`) and `RunSVD`. We then integrated RNA and ATAC modalities using
411 `FindMultiModalNeighbors` and `FindClusters` on the resulting joint weighted nearest-
412 neighbor graph to identify clusters. We used `FindAllMarkers` on the SCT assay and
413 separately on the ADT assay to report marker genes and proteins per cluster. We used these
414 markers to annotate the T cell phenotypes.

415

416 **Motif Accessibility Analysis**

417 We used the `RunChromVAR` function with default parameters from the Signac package to
418 compute transcription factor (motif activities from single-cell chromatin accessibility data. Briefly,
419 it quantifies how accessible each cell is at genomic regions associated with specific TF motifs
420 by comparing observed accessibility to background expectations. ChromVAR generates bias-
421 corrected, normalized activity scores (z-scores) for each motif in each cell, enabling the
422 identification of TFs that are potentially driving differences in chromatin states across cell
423 populations or experimental conditions. With the accessibility scores at hand, we used the
424 `FindMarkers` function to compute the differentially accessible markers per cell type (with
425 parameters `mean.fxn = rowMeans` and `fc.name = "avg_diff"`).

426

427 **KLF2 Targets**

428 We first extracted KLF2's motif's binding sites that overlapped with any identified peak. We used
429 the motif MA1515.2.[17] We then filtered for regions that were within 1000bp of a protein coding
430 gene's promoter to identify putative target genes. Among these genes, we reported those with a
431 log-fold-change (between the KLF2 over expression versus the empty vector conditions) of
432 above 1.0 or below –1.0 and a gene expression value of 0.1 in at least one of the conditions.
433

434 **LFA-1 dependent T cell priming assay**

435 *Cell Isolation*

436 OT-I T cells and dendritic cells were isolated as follows: for DC isolation, spleens from C57/Bl6
437 mice were minced and incubated in digestion buffer (200X DNase, 50X Liberase, RPMI) for 30
438 minutes at 37 degrees. During this incubation period, spleens from OT-I mice were isolated,
439 mashed over a 40 µm strainer. Subsequently, spleens were washed with RPMI and treated with
440 hypotonic ACK lysis buffer to lyse red blood cells. RBC lysis was quenched with 10x excess
441 PBS and centrifuged. OT-I T cells and DCs were then enriched using T-cell isolation
442 (Dynabeads™ Untouched™ Mouse T Cells Kit) and DC enrichment kits (Dynabeads™ Mouse
443 DC Enrichment kit), respectively. These are both negative selection kits in which cell
444 suspensions were first incubated with antibodies for 20 minutes at 4 degrees, subsequently
445 incubated with magnetic beads for 15 minutes with gentle tilting and rotation, and finally placed
446 on a magnet after which suspensions containing OT-I T cell and dendritic cell-enriched
447 populations were transferred to a fresh tube for downstream assays.
448

449 *T cell-DC coculture*

450 After isolation, DCs were resuspended in complete RPMI-1640 media containing 10% FBS, 2
451 mM L-glutamine and Pen/Strep and incubated at 37 degrees for 1 hour with gentle rotation in
452 the presence of escalating doses of SIINFEKL (N4), SIIQFEKL (Q4), SIITFEKL (T4), or

453 SIIVFEKL (V4) ranging from 0.1, 1, 10, and 100 nM. Cells were subsequently washed and
454 resuspended at 1 million cells/mL.
455
456 During this period, OT-I T cells were labeled with CellTrace Violet by resuspending in PBS at 1
457 million cells/mL, warming to 37 degrees, mixing 1:1 with CellTrace Violet diluted 1:1000 in pre-
458 warmed PBS and incubating in a 37 degree water bath for 20 minutes. Labeling was quenched
459 by adding 5x volume of RPMI+++. Labeled T cells were counted, centrifuged and resuspended
460 in complete T cell media (RPMI+++ containing 50 uM BME and 10 ng/mL IL-2) at 200K/mL, with
461 either isotype control (rat IgG2a kappa, BioXCell) or anti-LFA-1 (M17/4, BioXCell) at a final
462 concentration of 5 ug/mL. 500 uL containing 100K T cells were added to each well of a 96 well
463 Polypropylene Deep Well Plate (Corning) into which 5 uL DCs (5,000 DC total) were added. The
464 plate was then incubated at 37 degrees for 4 days.

465 For interrogation of cytokine production, PMA and ionomycin were added to wells to a final
466 concentration of 50 ng/mL and 500 ng/mL, respectively. 1 hour after addition of PMA and
467 ionomycin, Brefeldin A was added at a 1:1000 dilution and cells were incubated for another 3
468 hours, after which they were harvested and stained with surface antibodies as described above
469 using the panel below. Fixation was performed using an eBioscience FoxP3
470 Fixation/Permeabilization kit and stained overnight with intracellular antibodies diluted in
471 permeabilization buffer overnight at 4C. Data was acquired using a Cytek Aurora spectral
472 cytometer.

Staining type	**Marker**	**Fluorophore**	**Catalog #**	**Clone**	**Dilution**
Restimulation, Surface	B220	BUV496	BD Biosciences 612950	RA3-6B2	1:800
	TCRb	BUV805	BD Biosciences 748405	H57-597	1:100
	NK1.1	BUV615	BD Biosciences 751111	PK136	1:50

	CD4	BUV563	BD Biosciences 612923	GK1.5	1:800
	CD8	BV650	Biolegend 100741	53-6.7	1:800
	CD62L	BV570	Biolegend 104433	ME-14	1:200
	CD44	BUV737	BD Biosciences 612799	IM7	1:400
	PD-1	APC-Cy7	Biolegend 135224	29F.1A12	1:200
	CD39	BUV395	BD Biosciences 567264	Y23-1185	1:800
	CD25	PE	Biolegend 102008	PC61	1:200
	CD127	PE-Cy5	Biolegend 135015	A7R34	1:200
	CD69	PerCP-Cy5.5	Biolegend 104522	H1.2F3	1:200
	CX3CR1	APC	Biolegend 149008	SA011F11	1:400
	CXCR6	PE-Dazzle594	Biolegend 151117	SA051D1	1:200
Restimulation, Intracellular	IL-2	BV711	Biolegend 503837	JES6-5H4	1:800
	TNF	FITC	Biolegend 506304	MP6-XT22	1:800
	IFN-g	PE-Cy7	Biolegend 505826	XMG1.2	1:1600
	Granzyme B	Alexa 700	Biolegend 372222	QA16A02	1:3200

Methods Reference Section:

1 Amin, M., Edge, S., Greene, F. & et al. *AJCC Cancer Staging Manual*. 8th edn, (Springer, 2017).

2 Lauren, P. The Two Histological Main Types of Gastric Carcinoma: Diffuse and So-Called Intestinal-Type Carcinoma. An Attempt at a Histo-Clinical Classification. *Acta Pathol Microbiol Scand* **64**, 31-49 (1965). https://doi.org/10.1111/apm.1965.64.1.31

3 Cancer Genome Atlas Research, N. Comprehensive molecular characterization of gastric adenocarcinoma. *Nature* **513**, 202-209 (2014). https://doi.org/10.1038/nature13480

4 NCCN®. *NCCN Guidelines® Gastric Cancer 2.2023*, <https://www.nccn.org/guidelines/guidelines-detail?category=1&id=1434> (2023).

5 Herrera-Almario, G., Patane, M., Sarkaria, I. & Strong, V. E. Initial report of near-infrared fluorescence imaging as an intraoperative adjunct for lymph node harvesting during

robot-assisted laparoscopic gastrectomy. *Journal of Surgical Oncology* **113**, 768-770 (2016). https://doi.org/10.1002/jso.24226

6 Stoeckius, M. *et al.* Cell Hashing with barcoded antibodies enables multiplexing and doublet detection for single cell genomics. *Genome Biology* **19** (2018). https://doi.org/10.1186/s13059-018-1603-1

7 Germain, P.-L., Lun, A., Garcia Meixide, C., Macnair, W. & Robinson, M. D. Doublet identification in single-cell sequencing data using scDblFinder. *F1000Research* **10**, 979 (2022). https://doi.org/10.12688/f1000research.73600.2

8 Wolf, F. A., Angerer, P. & Theis, F. J. SCANPY: large-scale single-cell gene expression data analysis. *Genome Biology* **19** (2018). https://doi.org/10.1186/s13059-017-1382-0

9 Korsunsky, I. *et al.* Fast, sensitive and accurate integration of single-cell data with Harmony. *Nature Methods* **16**, 1289-1296 (2019). https://doi.org/10.1038/s41592-019-0619-0

10 Leland McInnes, J. H., James Melville. UMAP: Uniform Manifold Approximation and Projection for Dimension Reduction. https://doi.org/10.48550/arxiv.1802.03426

11 Cui, A. *et al.* Dictionary of immune responses to cytokines at single-cell resolution. *Nature* (2023). https://doi.org/10.1038/s41586-023-06816-9

12 Jin, S. *et al.* Inference and analysis of cell-cell communication using CellChat. *Nature Communications* **12** (2021). https://doi.org/10.1038/s41467-021-21246-9

13 Chandrasekaran, R. & Tamir, A. Open questions concerning Weiszfeld's algorithm for the Fermat-Weber location problem. *Mathematical Programming* **44**, 293-295 (1989). https://doi.org/10.1007/bf01587094

14 Lambert, S. A. *et al.* The Human Transcription Factors. *Cell* **172**, 650-665 (2018). https://doi.org/10.1016/j.cell.2018.01.029

15 Takashima, Y. *et al.* Resetting Transcription Factor Control Circuitry toward Ground-State Pluripotency in Human. *Cell* **158**, 1254-1269 (2014). https://doi.org/10.1016/j.cell.2014.08.029

16 Mimitou, E. P. *et al.* Scalable, multimodal profiling of chromatin accessibility, gene expression and protein levels in single cells. *Nature Biotechnology* **39**, 1246-1258 (2021). https://doi.org/10.1038/s41587-021-00927-2

17 Rauluseviciute, I. *et al.* JASPAR 2024: 20th anniversary of the open-access database of transcription factor binding profiles. *Nucleic Acids Research* **52**, D174-D182 (2024). https://doi.org/10.1093/nar/gkad1059

Figure 1

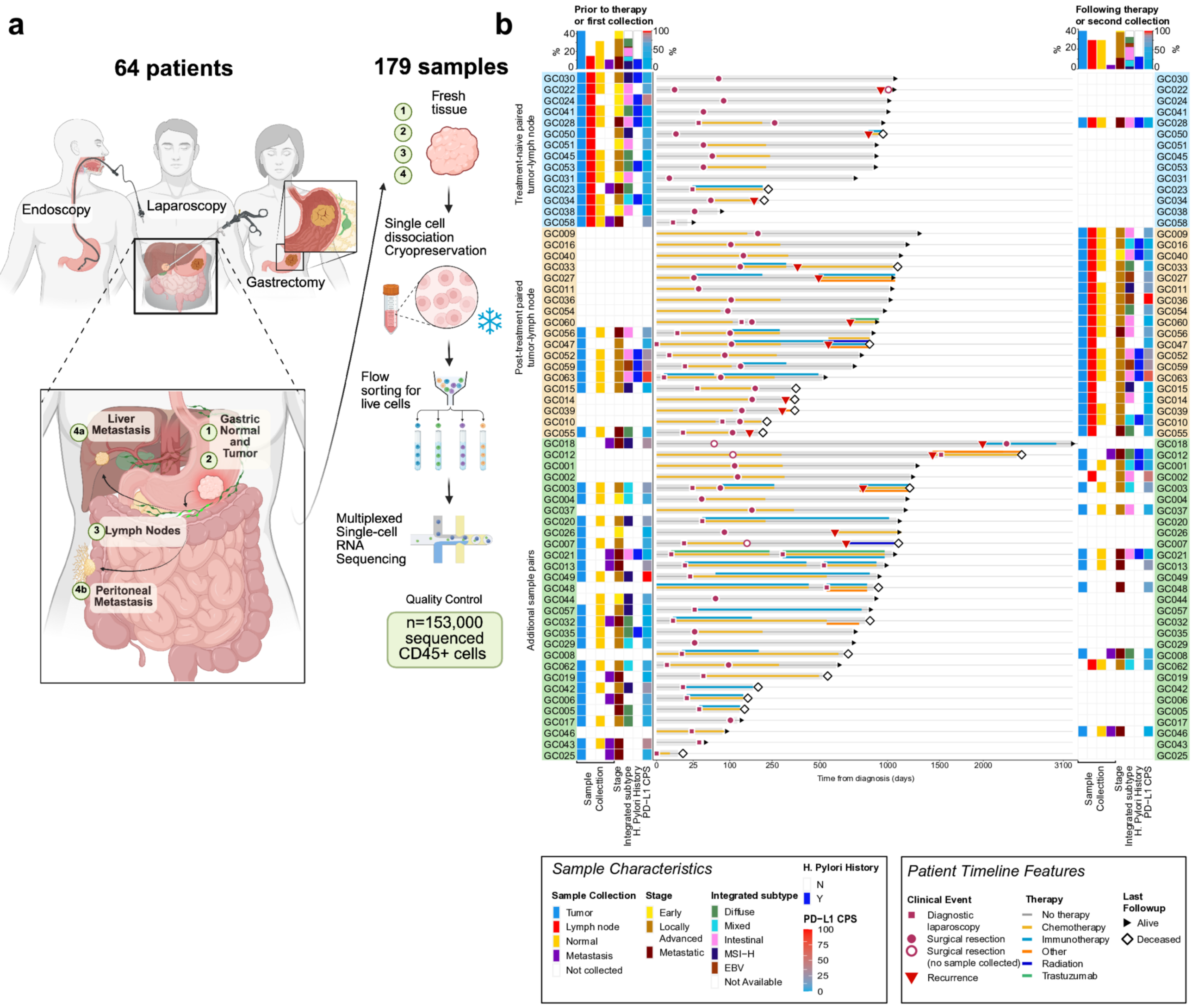
a
64 patients
179 samples
Endoscopy
Laparoscopy
Gastrectomy
Liver Metastasis
Gastric Normal and Tumor
Lymph Nodes
Peritoneal Metastasis
Fresh tissue
Single cell dissociation Cryopreservation
Flow sorting for live cells
Multiplexed Single-cell RNA Sequencing
Quality Control
n=153,000 sequenced CD45+ cells
b
Prior to therapy or first collection
Following therapy or second collection
Treatment-naive paired tumor-lymph node
Post-treatment paired tumor-lymph node
Additional sample pairs
Time from diagnosis (days)
Sample Collection
Stage
Integrated subtype
H. Pylori History
PD-L1 CPS
Sample Characteristics
Sample Collection
Tumor
Lymph node
Normal
Metastasis
Not collected
Stage
Early
Locally Advanced
Metastatic
Integrated subtype
Diffuse
Mixed
Intestinal
MSI-H
EBV
Not Available
H. Pylori History
N
Y
PD-L1 CPS
Patient Timeline Features
Clinical Event
Diagnostic laparoscopy
Surgical resection
Surgical resection (no sample collected)
Recurrence
Therapy
No therapy
Chemotherapy
Immunotherapy
Other
Radiation
Trastuzumab
Last Followup
Alive
Deceased

Figure 2

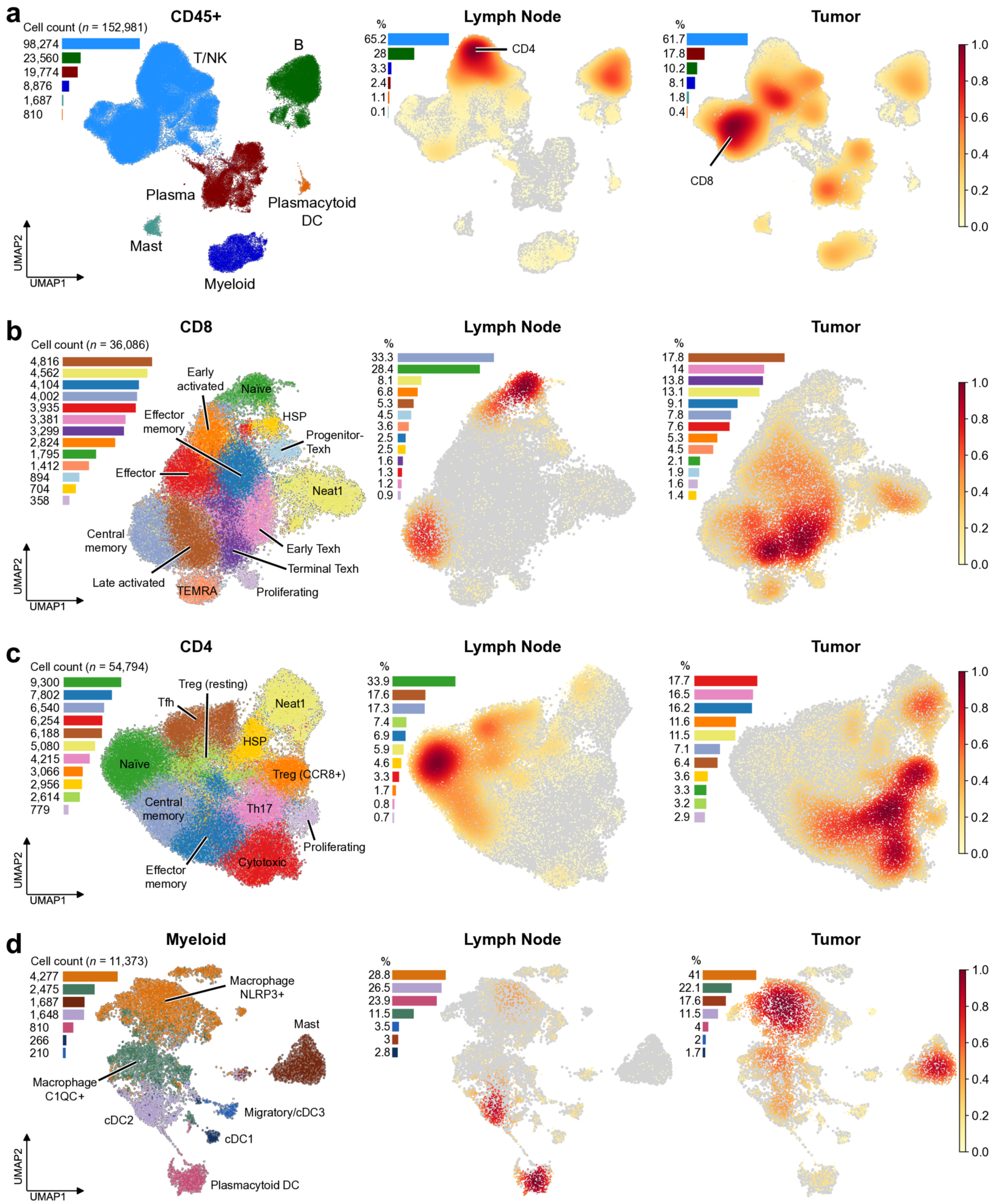
a
CD45+
Cell count (n = 152,981)
98,274
23,560
19,774
8,876
1,687
810
T/NK
B
Plasma
Plasmacytoid DC
Mast
Myeloid
UMAP2
UMAP1
Lymph Node
%
65.2
28
3.3
2.4
1.1
0.1
CD4
Tumor
%
61.7
17.8
10.2
8.1
1.8
0.4
CD8
1.0
0.8
0.6
0.4
0.2
0.0
b
CD8
Cell count (n = 36,086)
4,816
4,562
4,104
4,002
3,935
3,381
3,299
2,824
1,795
1,412
894
704
358
Early activated
Naïve
Effector memory
HSP
Progenitor-Texh
Effector
Neat1
Central memory
Early Texh
Terminal Texh
Late activated
TEMRA
Proliferating
UMAP2
UMAP1
Lymph Node
%
33.3
28.4
8.1
6.8
5.3
4.5
3.6
2.5
2.5
1.6
1.3
1.2
0.9
Tumor
%
17.8
14
13.8
13.1
9.1
7.8
7.6
5.3
4.5
2.1
1.9
1.6
1.4
1.0
0.8
0.6
0.4
0.2
0.0
c
CD4
Cell count (n = 54,794)
9,300
7,802
6,540
6,254
6,188
5,080
4,215
3,066
2,956
2,614
779
Treg (resting)
Tfh
Neat1
HSP
Naïve
Treg (CCR8+)
Central memory
Th17
Proliferating
Effector memory
Cytotoxic
UMAP2
UMAP1
Lymph Node
%
33.9
17.6
17.3
7.4
6.9
5.9
4.6
3.3
1.7
0.8
0.7
Tumor
%
17.7
16.5
16.2
11.6
11.5
7.1
6.4
3.6
3.3
3.2
2.9
1.0
0.8
0.6
0.4
0.2
0.0
d
Myeloid
Cell count (n = 11,373)
4,277
2,475
1,687
1,648
810
266
210
Macrophage NLRP3+
Mast
Macrophage C1QC+
Migratory/cDC3
cDC2
cDC1
Plasmacytoid DC
UMAP2
UMAP1
Lymph Node
%
28.8
26.5
23.9
11.5
3.5
3
2.8
Tumor
%
41
22.1
17.6
11.5
4
2
1.7
1.0
0.8
0.6
0.4
0.2
0.0

Figure 3

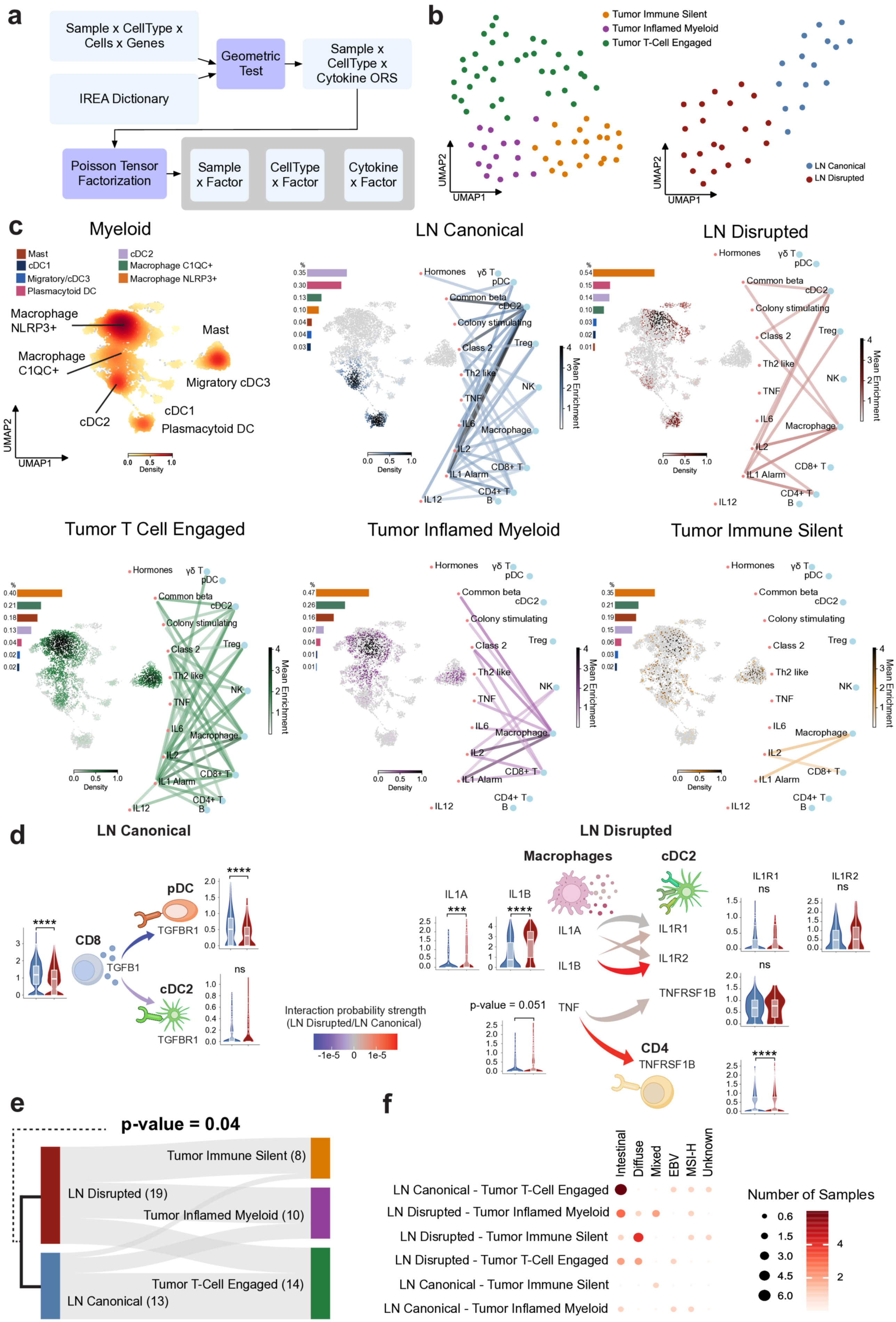
a
Sample x CellType x Cells x Genes
IREA Dictionary
Geometric Test
Sample x CellType x Cytokine ORS
Poisson Tensor Factorization
Sample x Factor
CellType x Factor
Cytokine x Factor
b
Tumor Immune Silent
Tumor Inflamed Myeloid
Tumor T-Cell Engaged
LN Canonical
LN Disrupted
UMAP1
UMAP2
c
Myeloid
LN Canonical
LN Disrupted
Mast
cDC1
Migratory/cDC3
Plasmacytoid DC
cDC2
Macrophage C1QC+
Macrophage NLRP3+
Density
Mean Enrichment
Tumor T Cell Engaged
Tumor Inflamed Myeloid
Tumor Immune Silent
d
LN Canonical
LN Disrupted
Macrophages
cDC2
CD8
pDC
cDC2
TGFB1
TGFBR1
IL1A
IL1B
IL1R1
IL1R2
TNFRSF1B
TNF
CD4
p-value = 0.051
Interaction probability strength (LN Disrupted/LN Canonical)
e
p-value = 0.04
Tumor Immune Silent (8)
LN Disrupted (19)
Tumor Inflamed Myeloid (10)
Tumor T-Cell Engaged (14)
LN Canonical (13)
f
Intestinal
Diffuse
Mixed
EBV
MSI-H
Unknown
LN Canonical - Tumor T-Cell Engaged
LN Disrupted - Tumor Inflamed Myeloid
LN Disrupted - Tumor Immune Silent
LN Disrupted - Tumor T-Cell Engaged
LN Canonical - Tumor Immune Silent
LN Canonical - Tumor Inflamed Myeloid
Number of Samples

Figure 4

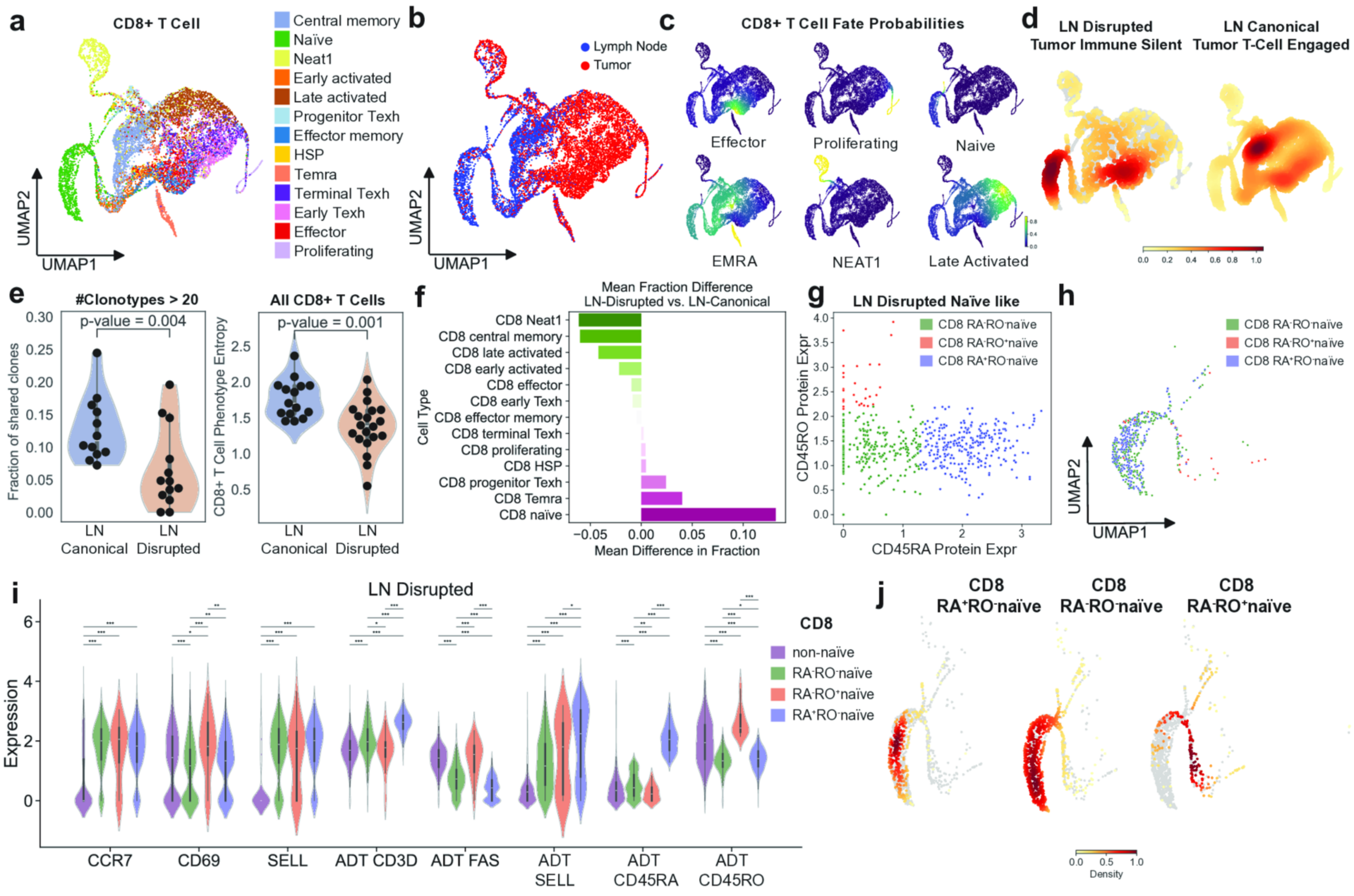
a
CD8+ T Cell
Central memory
Naïve
Neat1
Early activated
Late activated
Progenitor Texh
Effector memory
HSP
Temra
Terminal Texh
Early Texh
Effector
Proliferating
UMAP2
UMAP1
b
Lymph Node
Tumor
UMAP2
UMAP1
c
CD8+ T Cell Fate Probabilities
Effector
Proliferating
Naive
EMRA
NEAT1
Late Activated
d
LN Disrupted
Tumor Immune Silent
LN Canonical
Tumor T-Cell Engaged
0.0 0.2 0.4 0.6 0.8 1.0
e
#Clonotypes > 20
p-value = 0.004
Fraction of shared clones
LN Canonical
LN Disrupted
All CD8+ T Cells
p-value = 0.001
CD8+ T Cell Phenotype Entropy
LN Canonical
LN Disrupted
f
Mean Fraction Difference
LN-Disrupted vs. LN-Canonical
Cell Type
CD8 Neat1
CD8 central memory
CD8 late activated
CD8 early activated
CD8 effector
CD8 early Texh
CD8 effector memory
CD8 terminal Texh
CD8 proliferating
CD8 HSP
CD8 progenitor Texh
CD8 Temra
CD8 naïve
Mean Difference in Fraction
g
LN Disrupted Naïve like
CD8 RA-RO-naïve
CD8 RA-RO+naïve
CD8 RA+RO-naïve
CD45RO Protein Expr
CD45RA Protein Expr
h
CD8 RA-RO-naïve
CD8 RA-RO+naïve
CD8 RA+RO-naïve
UMAP2
UMAP1
i
LN Disrupted
Expression
CCR7
CD69
SELL
ADT CD3D
ADT FAS
ADT SELL
ADT CD45RA
ADT CD45RO
CD8
non-naïve
RA-RO-naïve
RA-RO+naïve
RA+RO-naïve
j
CD8 RA+RO-naïve
CD8 RA-RO-naïve
CD8 RA-RO+naïve
0.0 0.5 1.0
Density

Figure 5

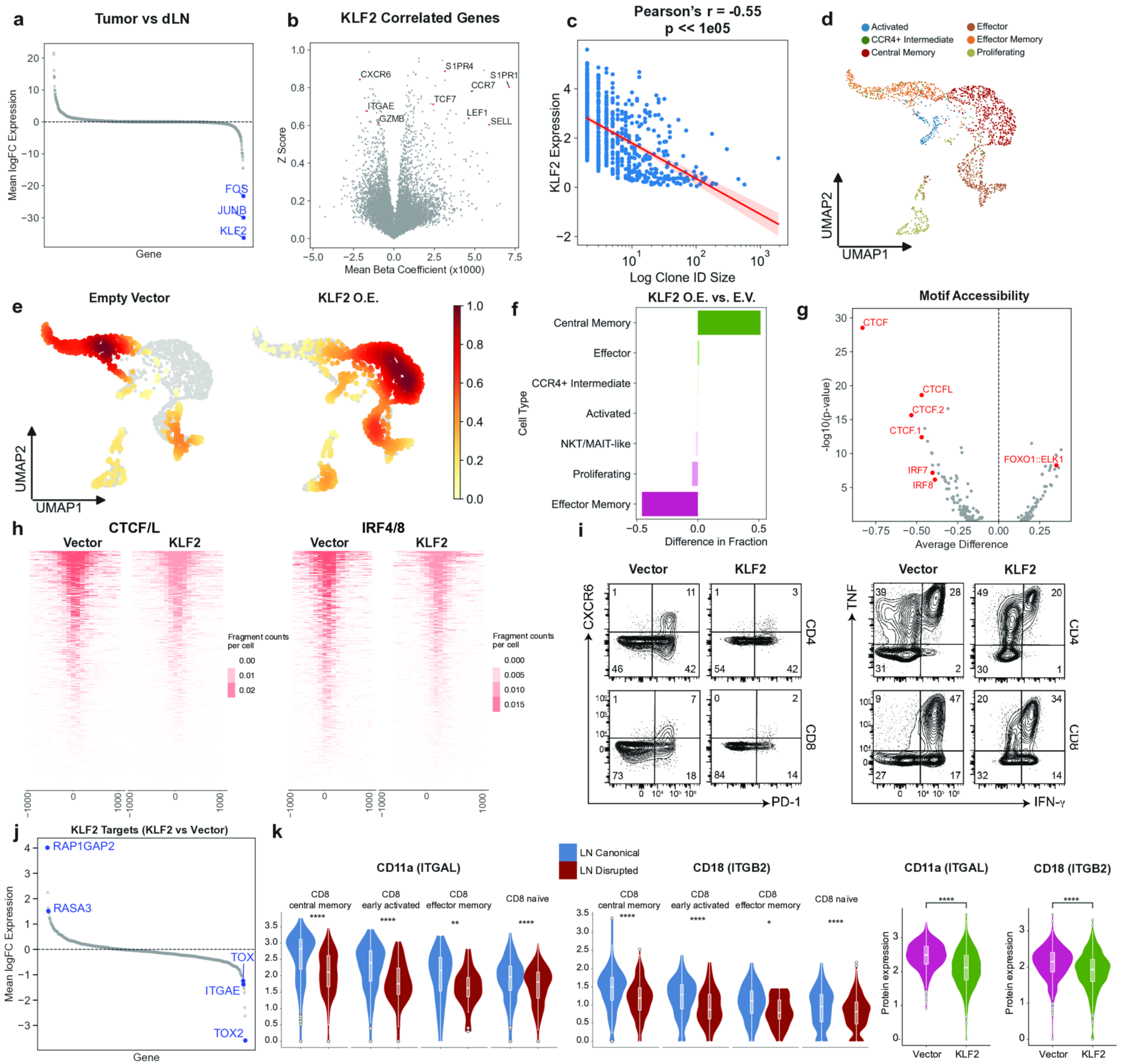
a
Tumor vs dLN
Mean logFC Expression
Gene
FOS
JUNB
KLF2
b
KLF2 Correlated Genes
Z Score
Mean Beta Coefficient (x1000)
CXCR6
ITGAE
GZMB
TCF7
S1PR4
CCR7
S1PR1
LEF1
SELL
c
Pearson's r = -0.55
p << 1e05
KLF2 Expression
Log Clone ID Size
d
Activated
CCR4+ Intermediate
Central Memory
Effector
Effector Memory
Proliferating
UMAP2
UMAP1
e
Empty Vector
KLF2 O.E.
UMAP2
UMAP1
f
KLF2 O.E. vs. E.V.
Cell Type
Central Memory
Effector
CCR4+ Intermediate
Activated
NKT/MAIT-like
Proliferating
Effector Memory
Difference in Fraction
g
Motif Accessibility
-log10(p-value)
Average Difference
CTCF
CTCFL
CTCF.2
CTCF.1
IRF7
IRF8
FOXO1::ELK1
h
CTCF/L
IRF4/8
Vector
KLF2
Fragment counts per cell
i
Vector
KLF2
CXCR6
CD4
CD8
PD-1
TNF
IFN-γ
j
KLF2 Targets (KLF2 vs Vector)
Mean logFC Expression
Gene
RAP1GAP2
RASA3
TOX
ITGAE
TOX2
k
LN Canonical
LN Disrupted
CD11a (ITGAL)
CD18 (ITGB2)
CD8 central memory
CD8 early activated
CD8 effector memory
CD8 naïve
Protein expression
Vector
KLF2

Figure 6

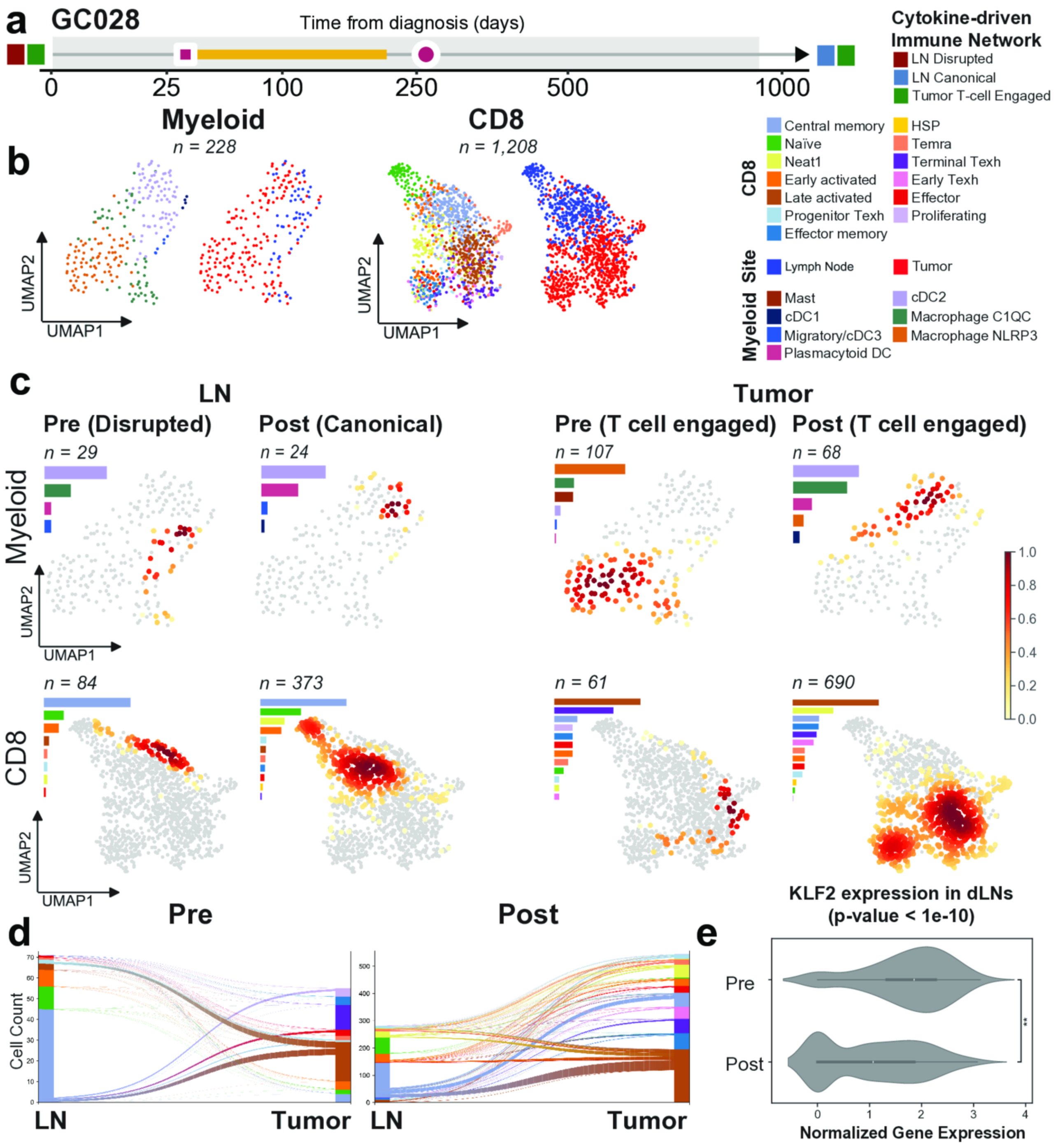
a
GC028
Time from diagnosis (days)
0
25
100
250
500
1000
Cytokine-driven Immune Network
LN Disrupted
LN Canonical
Tumor T-cell Engaged
b
Myeloid
n = 228
CD8
n = 1,208
UMAP2
UMAP1
CD8
Central memory
Naïve
Neat1
Early activated
Late activated
Progenitor Texh
Effector memory
HSP
Temra
Terminal Texh
Early Texh
Effector
Proliferating
Site
Lymph Node
Tumor
Myeloid
Mast
cDC1
Migratory/cDC3
Plasmacytoid DC
cDC2
Macrophage C1QC
Macrophage NLRP3
c
LN
Tumor
Pre (Disrupted)
Post (Canonical)
Pre (T cell engaged)
Post (T cell engaged)
n = 29
n = 24
n = 107
n = 68
Myeloid
n = 84
n = 373
n = 61
n = 690
CD8
1.0
0.8
0.6
0.4
0.2
0.0
Pre
Post
d
Cell Count
LN
Tumor
LN
Tumor
e
KLF2 expression in dLNs
(p-value < 1e-10)
Pre
Post
**
0
1
2
3
4
Normalized Gene Expression